Quasi-steady circulation regimes in the Baltic Sea

2   **Taavi Liblik[1], Germo Väli[1], Kai Salm[1], Jaan Laanemets[1], Madis-Jaak Lilover[1], Urmas Lips[1]**

4   [1]Department of Marine Systems, Tallinn University of Technology, Tallinn, Estonia

5   *** Correspondence:**
6   Taavi Liblik
7   taavi.liblik@taltech.ee

8   **Keywords: Circulation, ADCP, underwater glider, Baltic Sea, boundary current, geostrophic**
9   **current, upwelling-downwelling.**

10   **Abstract.** Circulation plays an essential role in the creation of physical and biogeochemical fluxes in
11   the Baltic Sea. The main aim of the work was to study the quasi-steady circulation patterns under
12   prevailing forcing conditions.

13   Six months of continuous vertical profiling and fixed-point measurements of currents, two monthly
14   underwater glider surveys, and numerical modeling were applied in the central Baltic Sea. The vertical
15   structure of currents was strongly linked to the location of the two pycnoclines: the seasonal
16   thermocline and the halocline. The vertical movements of pycnoclines and velocity shear maxima were
17   synchronous. The quasi-steady circulation patterns were in geostrophic balance and high-persistent.
18   The persistent patterns included circulation features such as upwelling, downwelling, boundary
19   current, and sub-halocline gravity current. The patterns had a prevailing zonal scale of 5–60 km and
20   considerably higher magnitude and different direction than the long-term mean circulation pattern.

21   Northward (southward) geostrophic boundary current in the upper layer was observed along the eastern
22   coast of the central Baltic in the case of southwesterly (northerly) wind. The geostrophic current at the
23   boundary was often a consequence of wind-driven, across-shore advection.

24   The sub-halocline quasi-permanent gravity current with a width of 10–30 km from the Gotland Deep
25   to the north over the narrow sill separating the Farö Deep and Northern Deep was detected in the
26   simulation, and it was confirmed by an Argo float trajectory. According to the simulation, a strong
27   flow, mostly to the north, with a zonal scale of 5 km occurred at the sill. This current is an important
28   deeper limb of the overturning circulation of the Baltic Sea. The current was stronger with northerly
29   winds and restricted by the southwesterly winds.

30   The circulation regime had an annual cycle due to seasonality in the forcing. Boundary current was
31   stronger and more frequent northward during the winter period. The sub-halocline current towards the
32   north was strongest in March–May and weakest in November–December.

1   Introduction

Current structure is an important player in the physical and biogeochemical fluxes in ocean. The semi-enclosed, shallow, brackish Baltic Sea has a strong but variable vertical stratification characterized by two pycnoclines: the permanent halocline and the seasonal thermocline (Leppäranta & Myrberg, 2009). Three-layer structure occurs in summer and consists of warm and less saline upper mixed layer, cold and saltier intermediate layer, and warmer and saltiest deep layer. Water column is mixed up to the permanent halocline at 60–80 m depth and cold intermediate water forms during winters. Stratification through the two pycnoclines impedes vertical mixing, and transport of substances between the layers is limited. The role of tides is marginal in the Baltic Sea. Lateral flows play an important role in distributing the water properties.

Water-mass circulation of the Baltic Sea is determined by the saline water inflow from the North Sea and freshwater input from the catchment area. The interaction of the fresher and saltier waters forms the Baltic haline conveyor belt (Döös et al., 2004). The belt consists of saltier water transport and signal propagation in the deep layer towards the north-eastern end of the Baltic (Liblik et al., 2018; Väli et al., 2013); upward salt flux through vertical mixing and transport (Reissmann et al., 2009), and outflow of the mix of riverine and saltier water in the upper layer (Jakobsen et al., 2010). The conveyor determines salinity, stratification and other important characteristics for the ecosystem.

The largest basin in the sea, the Baltic Proper (Fig. 1a) is a source for the deep waters of the Gulf of Riga, Gulf of Finland and Gulf of Bothnia. Permanent oxygen depletion has expanded in recent decades in the Baltic Sea, forming one of the largest dead zones in the global ocean (e.g. Carstensen et al., 2014). Only Major Baltic Inflows (Matthäus & Franck, 1992; Mohrholz, 2018) ventilate the deep layers of the southern and central Baltic Proper (Holtermann et al., 2017) but increase hypoxia in the Northern Baltic Proper and Gulf of Finland due to transport of former anoxic/hypoxic Eastern Gotland Basin water and stronger stratification (Liblik et al., 2018).

The basin-scale pattern of the long-term mean circulation in the Baltic Proper is cyclonic as demonstrated by several modeling studies (Hinrichsen et al., 2018; Jedrasik et al., 2008; Jędrasik & Kowalewski, 2019; Meier, 2007; Placke et al., 2018). The mean circulation is to the north along the eastern coast of the Baltic Proper and to the south along the eastern and western coast of Gotland Island (Meier, 2007; Placke et al., 2018). The turning area for this basin-wide cyclonic circulation cell in the north is between 59 to 59.5° N (Meier, 2007). The zonal center of the cyclonic flow in the Eastern Gotland Basin is in the Gotland Deep (Placke et al., 2018). The cyclonic structure exists from the bottom to the surface (Placke et al., 2018), although lateral structure and magnitude of the flow vary among different models (Placke et al., 2018). It is important to note that all aforementioned descriptors of the long-term mean flow rely on numerical simulations and lack support from observations. However, a consistent northward low-frequency current along the eastern slope of the Gotland Deep at 204 m depth has been reported (Hagen & Feistel, 2004). Placke et al. (2018) compared simulated currents with these measurements. All model simulations showed the mean meridional northward current velocity in the range of 0–1 cm s^{-1} (actually, three models out of four had values of 0.0–0.1 cm s^{-1}) while the measurements gave the mean northward velocity of 3 cm s^{-1} (Hagen & Feistel, 2004). Thus, the long-term mean flow to north in the deep layer was much stronger than the simulated mean current.

77 Temporal variability of currents in the Baltic Sea is very high as a reaction to atmospheric forcing.
78 Near-shore Eulerian current observations (Sokolov & Chubarenko, 2012) and drifter experiments
79 (Golenko et al., 2017; Krayushkin et al., 2019) conducted in the southern Baltic Proper showed a strong
80 correlation between wind and surface currents. Current velocity spectra in the Baltic include seiches
81 and tides with different periods from 11 h to 31 h and inertial motions with a period of about 14 h
82 (Jönsson et al., 2008; Lilover et al., 2011; Suhhova et al., 2018).

83 The vertical current structure through thermocline and halocline has not been rigorously studied by the
84 in-situ observations in the Baltic Proper. Moreover, despite a considerable effort to reveal the spatial,
85 long-term mean circulation patterns based on the simulations, not much has been done to study
86 temporal developments of currents in the synoptic (mesoscale) and seasonal timescales in the Baltic
87 Proper. In the present work, we address this shortage of knowledge.

88 Permanent circulation systems, such as boundary currents or subtropical gyres, are key processes that
89 determine transport in the open ocean (e.g. Macdonald, 1998). Although there are no permanent
90 currents in the Baltic Sea, we hypothesize that under stable wind forcing and stratification conditions,
91 a steady circulation regime prevails in the time-scale of days to weeks and has a much greater
92 magnitude than the mean current structures. These quasi-steady circulation features could be related to
93 the downwelling and upwelling processes or appear as a boundary current or a gravity current under
94 the halocline.

95 Following a description of the methods used, we present an analysis of (1) boundary current under
96 variable wind forcing and stratification, (2) quasi-permanent circulation patterns, and (3) sub-halocline
97 current. The analysis of observational and simulation results is followed by discussion and conclusions.

98
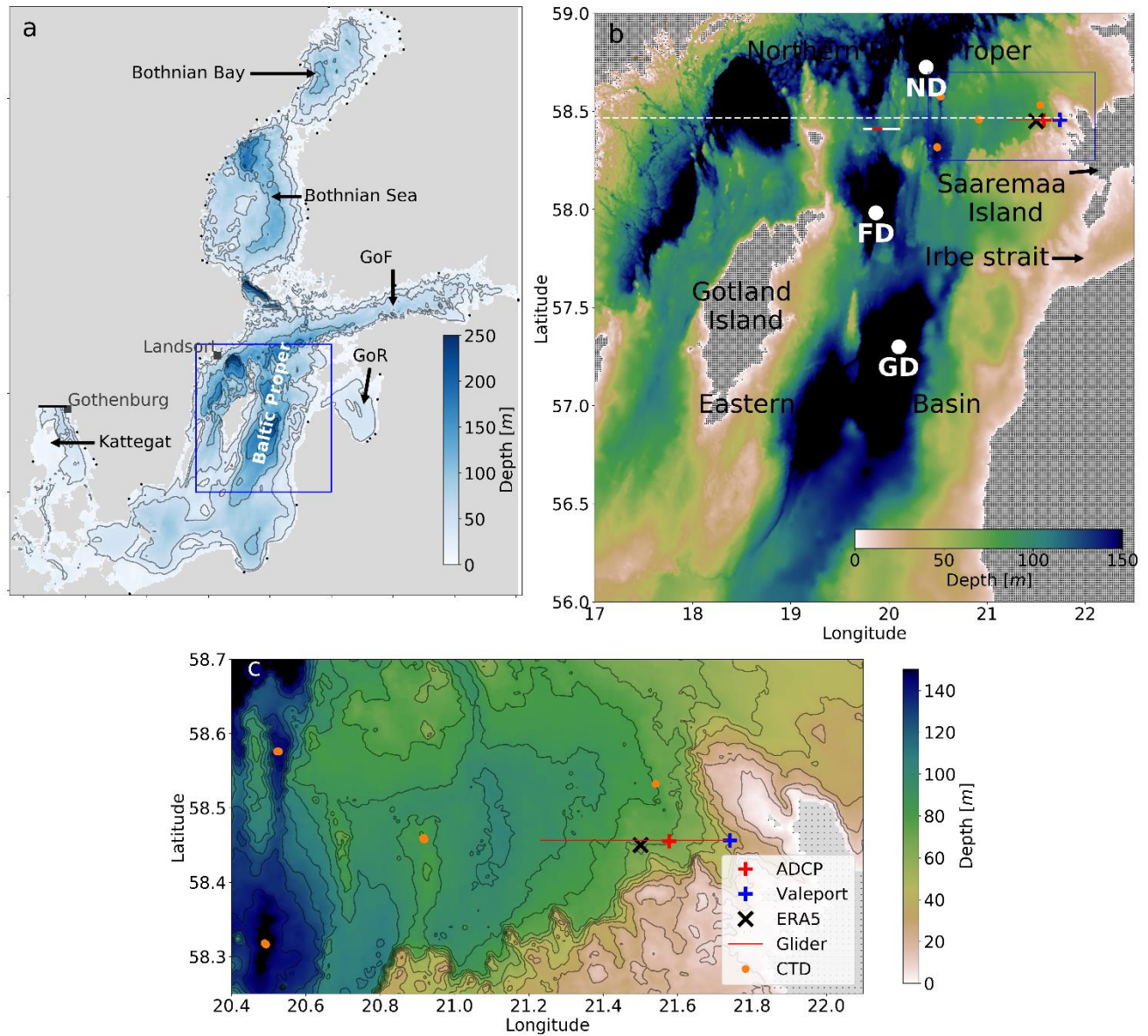
Figure 1. (a) Map of the Baltic sea and model domain. Shown are the locations of the open boundary of the model domain in the Kattegat (bold black line), Landsort and Gothenburg sea level stations, Baltic Sea rivers used in the model (black dots) and study area (blue box). (b) Close-up of the study area. Locations of ADCP and Valeport moorings, CTD measurements, glider section, the center of the cell of ERA5 wind data, and zonal section along the latitude of the ADCP location in the Nortern Baltic Proper (white dashed line) are presented. Gotland Deep (GD), Fårö Deep (FD) and Northern Deep (ND) are also shown. White line marks the section in Fig. 14a, and red line indicates time-series calculation range for Fig. 14b–c. (c) Close view of the moorings and CTD measurement locations, glider section, and local topography are shown. Dots on land (b, c) illustrate the model grid.

108

2   Data and methods

2.1 Observations and data products

111   A bottom mounted current profiler ADCP 300 kHz (Teledyne RDI) and model 106 current meter
112   (Valeport Ltd) (hereinafter referred to as Valeport) were deployed at the end of February 2020 to the
113   west of Saaremaa Island (Fig. 1b and c). Valeport was mounted at 5 m depth, while the sea bottom
114   depth in its location (58° 27.4' N, 21° 44.4' E) was 41 m. The sea depth in the ADCP location (58°
115   27.3' N, 21° 34.6' E) was 71 m and velocities were measured with vertical depth interval of 2 m in the
116   depth range of 10–68 m. Current velocity profiles were recorded as average of 1 h. The quality of the
117   current velocity data was checked following the procedure developed by Book (et al., 2007). Valeport
118   recorded current velocity with 10 min intervals. A Seabird SBE 16*Plus* V2 CTD SEACAT conductivity
119   and temperature recorder was deployed together with the ADCP, but it hung 4 m above the sea bottom,
120   i.e., at a depth of 67 m. SBE 16*Plus* sensors were calibrated by the manufacturer before the deployment.

121   Repeated CTD profiles onboard R/V Salme were collected using an OS320 CTD probe (Idronaut S.r.l.)
122   in the Northern Baltic Proper (see Fig. 1b and c) from 30 January to 4 August 2020.

123   Argo float deployment was arranged by the Finnish Meteorological Institute (Siiriä et al., 2019) from
124   15 August 2013 to 15 August 2014 and the trajectory data was derived from the Argo-based deep
125   displacement dataset (Ollitrault & Rannou, 2013). The dataset was downloaded on 15 March 2021 at
126   https://www.seanoe.org/data/00360/47077/.

127   In 2020, two glider missions were conducted in the Northern Baltic Proper. The Slocum G2 Glider
128   collected oceanographic data along the E–W oriented 27 km long section (Fig. 1b and c). The
129   easternmost point of the glider track was approximately 7 km off the shoreline and the section was
130   located at the sloping bottom where sea depth gradually deepened westward from 40 m to 90 m. The
131   first mission was carried out from 28 February to 22 March 2020 and the second one from 4 August to
132   2 September 2020. Both ascending and descending profiles were recorded and altogether over 8000
133   profiles were gathered. The glider moved at a horizontal speed of 0.33 ± 0.08 m s^{-1}. On average, a profile
134   took 8.0 ± 0.9 min to complete 80–90 m deep profile and the average distance between the profiles near
135   the surface was 301 ± 46 m. Both the sampling time and the distance were decreased by half in the
136   shallow part of the section.

137   Preliminary glider data processing included the standard quality control (impossible date and location
138   test, range tests for the sensors; practically no incorrect data were detected) and accounting for the
139   response time of the sensors and the thermal lag. First, a linear time shift was applied to temperature
140   and conductivity considering the misalignment with pressure. Temperature was re-aligned by 1.4 s and
141   conductivity by 0.9 s for the mission conducted in the spring and respectively by 1.6 s and 1.1 s for the
142   mission in the summer. The parameters were chosen by comparing consecutive profiles focusing on
143   the depth range around the greatest gradient. It was assumed that successive profiles correspond to the
144   same water mass. We followed Mensah et al. (2009) to remove the thermal lag effect and found optimal
145   coefficients for the temperature error amplitude, α, and time constant, t_c, by comparing consecutive
146   TS-profiles. The satisfying results were obtained in the case of $\alpha = 0.0025$ and $t_c = 10$ s for the earlier
147   mission and $\alpha = 0.055$ and $t_c = 12$ s for the following one. The profiles were averaged on a 0.5 dbar
148   vertical grid after processing the raw data.

149

150   Sea surface temperature was derived from the Copernicus Marine Service product
151   SST_BAL_SST_L4_REP_OBSERVATIONS_010_016 with a horizontal resolution of 0.02 x 0.02
152   degrees. Mean difference between the product and in-situ data sources has been in the range of –0.12
153   to –0.21 °C and root mean square error from 0.43 to 0.88 °C depending on the data sources according

154 to the quality information document
155 (https://catalogue.marine.copernicus.eu/documents/QUID/CMEMS-SST-QUID-010-016.pdf,
156 accessed 19 August 2021).

157 Hourly, 10 m level wind velocities of ERA5 reanalysis data (Hersbach et al., 2020) at the cell with the
158 size 0.25°x0.25° from 1979 to 2020 (see Fig. 1 for location) were used in the analyses.

159

2.2 Modeling

161 Numerical model GETM (General Estuarine Transport Model, Burchard & Bolding, 2002) has been
162 applied to simulate the circulation and temperature/salinity distribution in the northeastern Baltic Sea.
163 GETM is a primitive equation, three-dimensional model with free surface and $k–\varepsilon$ turbulence model
164 for vertical mixing by coupling the hydrodynamic part with GOTM (General Ocean Turbulence Model,
165 Umlauf & Burchard, 2005).

166 Model domain covered the whole Baltic Sea with the open boundary situated in the Kattegat region
167 (Fig. 1a). The horizontal grid spacing of the model was 0.5 nautical miles (926 m) and 60 vertically
168 adaptive coordinates (Hofmeister et al., 2010; Gräwe et al., 2015) were used. Sea surface height from
169 Gothenburg station has been used as the boundary condition to control the barotropic in- and outflow
170 from the Baltic Sea, while the temperature and salinity were nudged towards monthly climatological
171 profiles (Janssen et al., 1999) along the open boundary.

172 Data from the Estonian version of the operational model HIRLAM (High Resolution Limited Area
173 Model) maintained by the Estonian Weather Service and giving forecasts with hourly resolution
174 (Männik and Merilain, 2007) were used to calculate the momentum and heat flux at the sea surface.
175 Climatological runoff of the Baltic Sea rivers with inter-annual variability added from the values
176 reported to the HELCOM (Johansson, 2016) was used. Simulation covered period from April 2010 to
177 September 2020, and initial temperature and salinity fields were taken from the CMEMS (Copernicus
178 Marine Service) re-analysis product for the Baltic Sea.

179 The same setup of the model was previously used in Zhurbas et al. (2018) and Liblik et al. (2020) and
180 more details about the model setup are given there. Zhurbas et al. (2018) validated the salinity and
181 temperature values in the central Baltic Sea along with the sea surface height at Landsort station and
182 compared the near-bottom current statistics with the long-term observations in the Gotland Deep.
183 Liblik et al. (2020) validated the simulated wintertime sea surface temperature and salinity in the Gulf
184 of Finland and compared the observed mixed layer depth with the simulations. In this study, we will
185 present the comparison of simulated and observed currents in the Northern Baltic Proper.

186

2.3 Calculations

188 Isohaline 9 g kg^{-1} was selected to define the center of the halocline (CH) depth since the halocline was
189 steepest around this salinity value according to the salinity profiles. Isoterm 13 °C was selected to
190 define the center of the thermocline depth using the same logic. Thermocline was defined only for the
191 second glider mission in August 2020.To estimate the center of halocline depth based on single level
192 salinity time-series measured by the SBE 16*Plus*, and twelve CTD profiles collected by the RV Salme
193 in the Northern Baltic Proper (see Fig. 1b) from 30 January to 4 August 2020 were used. Salinity

194   profiles were vertically normalized by subtracting the depth of the CH at each profile. Next, the mean
195   salinity profile in the normalized depth coordinates was calculated (Fig. 2). The mean normalized depth
196   and salinity relationship were used to derive the CH depth from the SBE 16*Plus* salinity time-series at
197   67 m depth. If salinity was lower (higher) than 9 g kg^{-1}, the CH was deeper (shallower) than 67 m
198   according to the mean depth-salinity curve (Fig. 2). Maximum depth of the neighboring sea area, 88
199   m, was defined as the maximum depth of the CH.

200   In this study the *x*-axis is positive eastward, the *y*-axis is positive northward, and the *z*-axis is positive
201   upward (*z*=0 at the sea surface), *u* and *v* are horizontal velocity components.

202   The baroclinic components of the geostrophic velocity (*u$_g$ and v$_g$*) can be deduced from the
203   hydrographic data. Considering the dynamic method, the geostrophic relationships are as follows

204    $v_g = \frac{1}{f}\frac{\partial \Phi}{\partial x}$

205    $u_g = -\frac{1}{f}\frac{\partial \Phi}{\partial y}$

206   The geopotential, Φ, is proportional to the dynamic height, D, as

207    $\Phi = gD$

208   where *g* is the gravitational acceleration and *f* is the Coriolis parameter.

209   The dynamic height can be determined from the temperature and salinity (density) profiles.

210   The relative geostrophic velocity was evaluated using dynamic height anomaly relative to a reference
211   pressure (McDougall & Barker, 2011). The geopotential slope of an isobaric surface expresses the
212   horizontal pressure gradient. A zonal glider track enabled to calculate the meridional velocity profile
213   of the geostrophic flow. The meridional geostrophic velocity was calculated also from the GETM
214   simulation data. The reference level was set at 70 dbar. The shallower profiles were included using the
215   stepped no-motion level method described in Rubio et al. (2009). Since velocity is not zero at the 70
216   dbar level, the calculated geostrophic velocities V$_{GEO-DENS-glider}$ and V$_{GEO-DENS-GETM}$ described in
217   subchapter 3.1 represent relative velocities to the no-motion 70 dbar level. Both variables represent an
218   averaged velocity at an extent of 10 km zonal scale around ADCP position.

219   To compare the simulated geostrophic velocity profiles with the measured ADCP velocity profiles, the
220   relative geostrophic velocity at the sea surface (calculated relative to 70 dbar using simulated density
221   profiles) was aligned with the geostrophic velocity due to the sea level gradient from the model
222   simulation (V$_{GEO-SL-GETM}$). Sea level gradient was estimated from linear regression fit of sea level
223   anomalies at a horizontal scale of 10 km. The difference (vector) between the density-estimated and
224   the sea level estimated geostrophic velocity at the sea surface was applied to the whole geostrophic
225   velocity profile under the assumption that the geostrophic current at the surface is determined by the
226   differences in the sea level exclusively. Adjusted geostrophic velocity profiles were presented as V$_{GEO-}$
227    $_{ADJ-GETM}$ in subchapter 3.2.

228
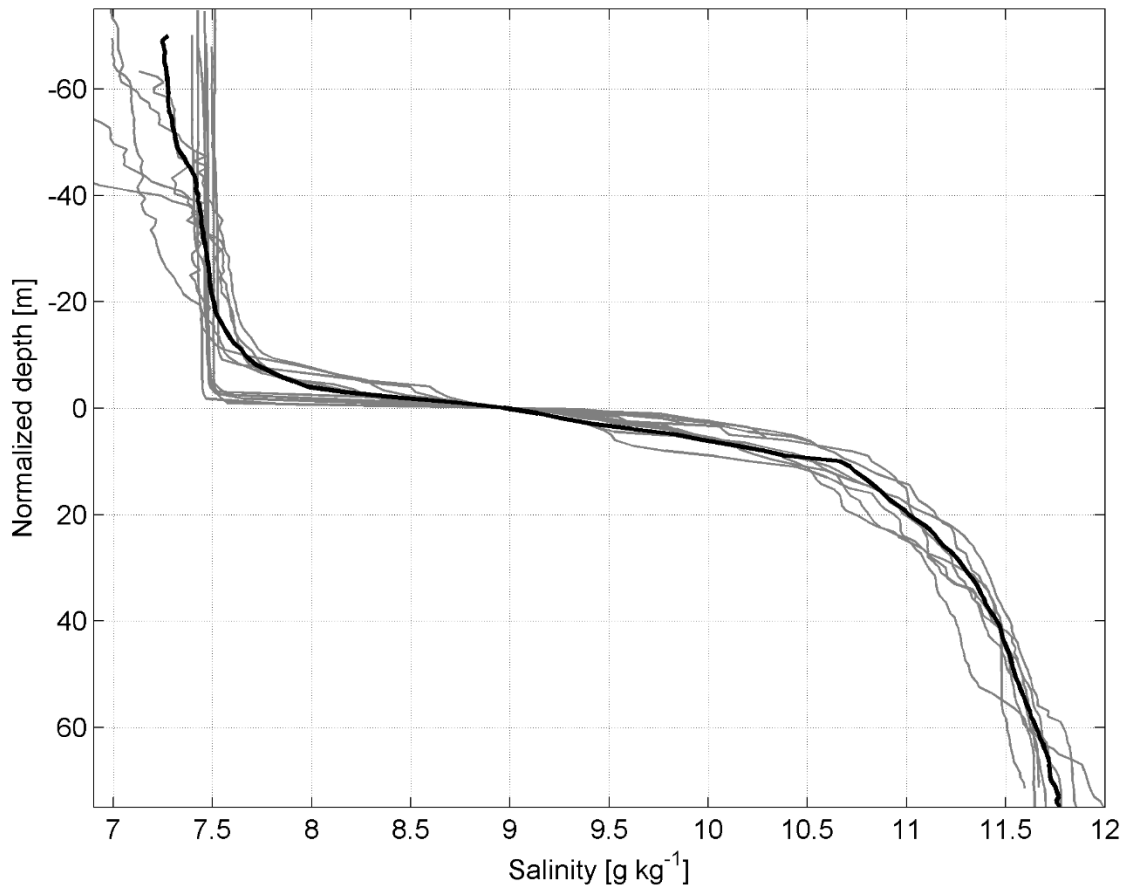
Figure 2. Vertically normalized salinity profiles from 30 January to 4 August 2020 in the Northern Baltic Proper (see Fig. 1b). Bold black line represents the mean salinity profile.

The direct influence of wind forcing on the subsurface currents was ascertained using the classical Ekman model based on the balance of the frictional and Coriolis forces (Ekman, 1905). Wind stress vector τ as the Ekman model input parameter was calculated using ERA5 (Fig. 1b and c) wind data: $\tau = \rho_{air}cd|\mathbf{U}|\mathbf{U}$, which were prior low-pass filtered with cut-off 36 hours to exclude periodic processes. Here $\mathbf{U}$ is the wind velocity vector at 10 m height, cd is the drag coefficient and was parameterized as proposed by (Wu, 1980): $cd=(0.8+0.065|\mathbf{U}|)\times10^{-3}$, $|\mathbf{U}|$ is the wind velocity vector module and ρ_{air} is the density of air. The eddy viscosity used in the model was calculated according to (Csanady, 1981): $\nu = |\tau|/200f$, where $|\tau|$ is the wind stress vector module. The model outputs are the vertical profiles of wind-induced current velocity components.

The temporal development in the vertical current structure is presented as the time-series of vertical current shear squared $s^2 = (\partial u/\partial z)^2 + (\partial v/\partial z)^2$.

Persistency of the current, characterizing the variability of the direction of the flow, is defined as the ratio between vector and scalar current speeds:

244 $$R = \frac{\sqrt{u^2+v^2}}{\frac{1}{N}\Sigma\sqrt{u_n^2+v_n^2}}.$$ Current and wind

245 velocity components are presented as 36-h and 10-day low-pass time-series. The fourth-order
246 Butterworth filter was used for low-pass filtering.

3 Results

3.1 Boundary current under variable wind forcing

249 Statistics of the 6 months (1 March–1 September 2020) ADCP current data revealed the persistency of
250 currents between 32 and 42%, with the highest persistency in the 20–40 m depth range (Table 1). Mean
251 and maximum hourly measured speeds were higher in the uppermost bin at 11 m depth, 11 and 48 cm
252 s^{-1}, respectively and lower in the near-bottom layer, 7 and 34 cm s^{-1}. The mean u- and v-components
253 were positive in all depths showing the mean flow to the NE sector.

254 From the flow structure point of view the ADCP current velocity time series can be divided into two
255 periods: 1) from March until mid-April, when barotropic regime prevailed, 2) from mid-April until
256 September, when layered flow dominated (Fig. 3a and b). One can also see the coincidence of the
257 current u- and v-components in the uppermost and deepest bin during the first period (Fig. 3c and d)
258 except a short period at the end of March. Discrepancies between the two layers afterwards illustrated
259 the layered, baroclinic nature of the flow. The flow regime reacted well to wind forcing. Barotropic
260 flow to the northeast prevailed as a result of southwesterly winds until mid-April (Fig. 4). Only during
261 the last week of March, when wind was from northerly directions, a strong southerly current was
262 observed. Similar temporal patterns appeared in the upper layer in the stratified period. Alteration of
263 positive and negative meridional velocities was related to the prevailing wind direction. These
264 tendencies were evident both in the ADCP and Valeport locations. Deep layer current was directed to
265 the east, i.e., onshore, when southerly flow occurred in the upper layer and to the west or southwest,
266 when the current to the northeast prevailed. These are signs of the layered structure of the coastal
267 upwelling and downwelling.

268 The most frequent current direction in the upper layer (at a depth of 11 m) was 40° at the ADCP
269 location. To estimate the relationship between the low-frequency (10-day low-pass) current component
270 and wind, we calculated the correlation between the 40° current velocity component (c_{40}) in the upper
271 layer and wind speed from different directions with different time lags. The best correlation (r^2=0.65,
272 p<10^{-100}, n=4473) was found with the wind from the south, specifically towards 10° (w_{10}), applying a
273 3-day time lag. This, on the one hand, corresponds to Ekman's theory, however, on the other hand, the
274 3-day delay is rather long. Probably it can be explained by the mixed effect of wind on the surface
275 currents. The momentum flux created by wind impacts the current field fast. The correlation without
276 delay is relatively high (r^2=0.55, p<10^{-100}, n=4473) as well. The flow resulting from the sea level
277 gradient and due to the inclination of isopycnal surfaces are also a consequence of wind but develop
278 slower.

279 Time series of c_{40} reveal negative values from mid-April until the end of June (Fig. 3e). Before mid-
280 March and in July–August, the c_{40} was mostly positive. The main course of w_{10} and c_{40} coincided well,
281 but discrepancies occurred in the details. For instance, negative c_{40} occurred when w_{10} was positive in
282 the ADCP location in the last third of March and first half of May. The mean values of w_{10} and c_{40}
283 during the measurements were 0.6 m s^{-1} and 3.2 cm s^{-1}, respectively. The w_{10} is higher in winter and
284 smaller in summer. Considering the linear relation between the two variables, the 1979–2020 mean
285 w_{10} = 1.1 m s^{-1} corresponds to c_{40} = 4.2 cm s^{-1}.

286 At the Valeport location, the most frequent current direction was 350°. The discrepancy between the
287 dominant flow direction at the ADCP and Valeport locations is related to the topographic features (Fig.
288 1). However, from the wider Baltic Sea dynamics point of view the meridional current component is
289 important to investigate. To study the temporal developments of the meridional current, we next
290 analyze the measured and simulated meridional current components at 11 m depth at the ADCP
291 location, V_{ADCP} and V_{GETM}. We also calculated the geostrophic meridional component $V_{GEO-SL-GETM}$ of
292 the current velocity from the simulated sea level gradient and relative geostrophic meridional current
293 component ($V_{GEO-DENS-GETM}$) at 11 m depth based on simulated temperature and salinity data in the
294 section. The relative geostrophic meridional component ($V_{GEO-DENS-glider}$) was calculated using the
295 glider temperature and salinity data as well. We also calculated mean Ekman current u- and v-
296 components in the depth range 0–10 m U_{Ekman} and V_{Ekman}, respectively. All parameters are 36-h low-
297 pass filtered.

298 Overall, the simulated V_{GETM} follows the temporal changes in measured V_{ADCP} reasonably well (Fig.
299 5). V_{GETM} tends to have smaller values than V_{ADCP}, which means that the meridional component of
300 simulated velocity is biased southward. Sometimes, e.g., in June and August, the discrepancies are
301 considerable. Geostrophic meridional current component $V_{GEO-DENS-GETM}$ was very small, and V_{GEO-}
302 $_{DENS-glider}$ was practically zero in March (Fig. 5b) as the water column was mixed down to the reference
303 depth of the geostrophic current calculation. Since the end of March, overall temporal developments
304 in the meridional current components (V_{ADCP} and V_{GETM}) and its geostrophic meridional components
305 ($V_{GEO-DENS-GETM}$), ($V_{GEO-SL-GETM}$) and $V_{GEO-DENS-glider}$) in August match quite well (Fig. 5a and b). This
306 can be related to the multiple effects of wind. South-westerly wind resulted in the Ekman current
307 towards the eastern coast of the Northern Baltic Proper. This caused, first, a sea level gradient across
308 the basin (higher near the coast), which induced barotropic current to the north. Secondly, it induced
309 downwelling along the coast and resulted in a vertical gradient of the geostrophic current. Such events
310 were detected at the beginning of April and July, when strong southwesterly winds blew (Fig. 4) and
311 caused Ekman current towards the coast (Fig. 5c). Northerly or northeasterly winds caused opposite
312 effects. Sea level was lower near the coast compared to offshore and thermocline was located at
313 shallower depths near the coast. Thus, the flow was directed to the south in the surface layer. Such
314 events occurred in late March and mid-August. Most of the major events of the positive V_{ADCP} and
315 V_{GETM} were associated with the positive u-component of the Ekman current (cf. Fig. 5a and c), i.e.,
316 flow towards the shore, not along the shore. Thus, the wind-driven strong coastal current to the north
317 is not induced by the direct momentum flux created by wind stress but rather is the result of wind-
318 driven sea level gradient and depression of the pycnoclines at the coast, which resulted in vertically
319 sheared geostrophic current.

320 Next, we consider the relationship between the vertical maxima of the current shear and the vertical
321 location of pycnoclines – seasonal thermocline and halocline. Seasonal thermocline began to develop
322 from the beginning of May (Fig. 6a). The temporal course of salinity at 67 m depth (Fig. 6b) and depth
323 of halocline center (Fig. 6d) showed that halocline was mostly located deeper than the deepest ADCP
324 bin. At the end of March, the halocline center reached 55 m depth (Fig. 6d) and high current shear
325 values were observed below 45 m depth (Fig. 6c). Shallower halocline was related to the northerly
326 wind event (Fig. 4), which caused offshore Ekman transport in the upper layer and compensating
327 onshore flow in the deep layer (Fig. 3). Such events of high current shear in the deep layer also occurred
328 at the end of April to early May, from the end of May to mid-June and in mid-August (Fig. 6c) when
329 the halocline center was shallower, and salinity increased at 67 m depth. Note that the depth of the
330 halocline center and shear maxima were vertically shifted, halocline center was deeper. This can be
331 explained by the vertical range of the halocline. The upper boundary of the halocline is shallower than

332 the center of the halocline. Thus, the shear maxima were rather linked to the upper boundary of the
333 halocline.

334 Stronger and more extensive shear maxima in the upper part of the water column were observed since
335 late April (Fig. 6c). It appeared days before thermal stratification developed. One could see that SST
336 (sea surface temperature) and temperature at 67 m depth coincided until the end of April. The
337 occurrence of earlier shear maxima could be explained by the formation of the stratification in the
338 upper layer caused by the transport of fresher surface water to the area due to northerly wind forcing.
339 Shear maxima became stronger in the second half of May when thermal stratification developed.
340 Strong downwelling and vertical mixing occurred in July as a result of a strong southwesterly wind
341 impulse with the duration of more than a week (Fig. 4). This can be seen as a drop in SST from 21 to
342 15 °C and occasional high temperature recordings in the deep layer (Fig. 6a). The latter indicates that
343 the upper layer water arrived at the 67 m deep measurement spot. This event is well reflected in the
344 time series of current shear. Deepening of the shear maxima down to 50–55 m depth (Fig. 6c) occurred
345 together with thermocline deepening, as the near-bottom temperature recordings suggest. A
346 precondition for such a rapid drop in SST was the formation of a thin and exceptionally warm surface
347 layer due to atmospheric heat flux (Fig. 6a) and weak wind (Fig. 4) at the end of June. Relaxation of
348 the downwelling occurred in mid-July, and another downwelling developed at the end of July. The
349 linkage between the thermocline and shear maxima was well seen in August when glider observations
350 were available (Fig. 6c). The thermocline and shear maxima reached down to 40 m depth in the
351 beginning and the end of the month, while they were located at 20 m depth in the middle of the month
352 (Fig. 6a and c). The vertical movements of the halocline (Fig. 6d) and thermocline (Fig. 6a and Fig.
353 6c) and linked shear maxima were synchronized. As thermocline, the halocline had its position also
354 shallower in mid-August and deeper before and after. Note that downwelling was initiated by strong
355 southerly, southwesterly or westerly winds and all events were seen as a SST decrease, likely due to
356 vertical mixing, decrease in salinity at 67 m depth and deepening of the thermocline and halocline and
357 related shear maxima. Relaxation of downwelling occurred when northerly winds or calmer periods
358 prevailed and appeared as an increase in SST and upward movement of both pycnoclines.

359 Thus, we can conclude that the vertical structure of currents was strongly linked to the varying depths
360 of pycnoclines, which were sensitive to wind forcing.

361 **Table 1.** Statistics of the 1-h average ADCP current data from 28 February to 2 September 2020.

Depth (m)	Mean speed (cm s^{-1})	Mean u (cm s^{-1})	Mean v (cm s^{-1})	Maximum speed (cm s^{-1})	Persistency (%)
10.8	11.3	3.8	1.1	48	35.1
20.8	10.2	4	1.7	44	42.3
30.8	9.5	3.7	1.4	38	41.7
40.8	9	3.4	1.1	37	40.1
50.8	8.8	2.9	0.8	35	34.5
60.8	8.3	2.7	0.7	36	34
66.8	7	1.9	1.2	34	32.7

362

363

364

365

366

367

368

369

370
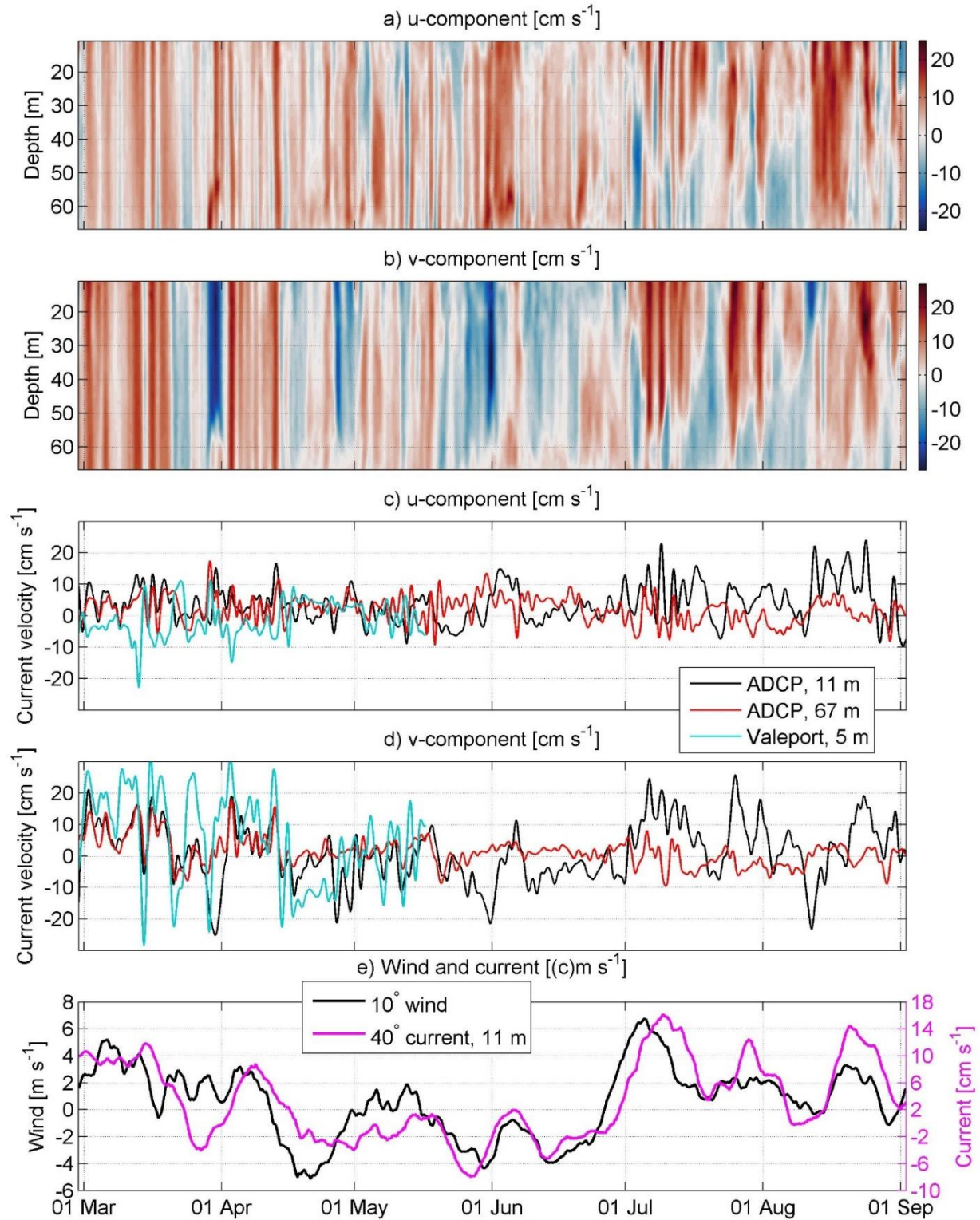
Figure 3. Temporal course of the low-pass filtered (36 h) current velocity *u*-component (positive eastward, a and c) and v-component (positive northward, b and d) in the water column (a, b); and in the upper (11 m depth) and deep layer (67 m depth, c, d) in the ADCP and Valeport locations in 2020 (Fig. 1). Low-pass filtered (10 days) wind 10°-component and current 40°-component at 11 m depth in the ADCP location (e).

375
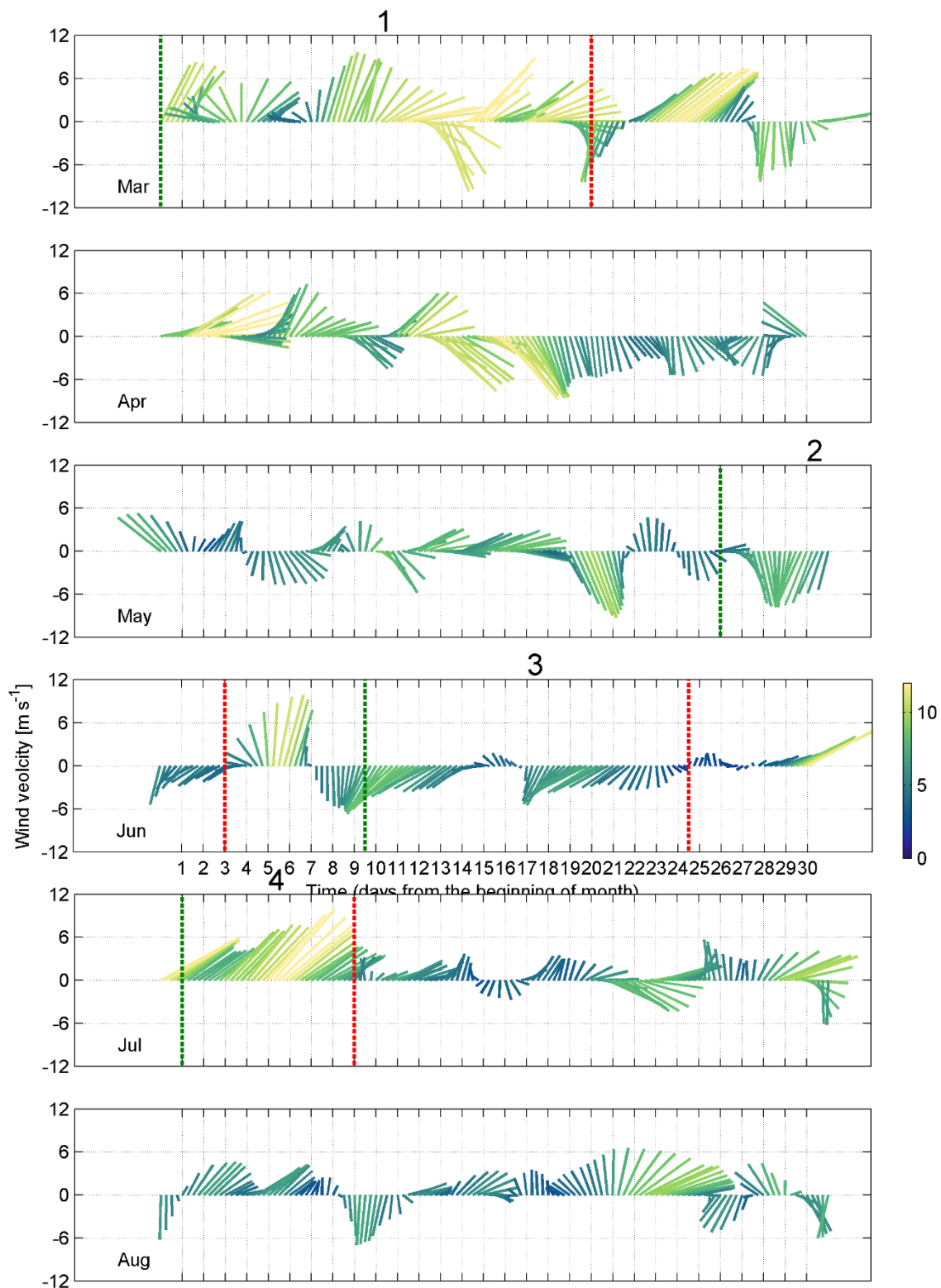
Figure 4. Time series of the 10-m level ERA5 wind data from 1 March to 31 August 2020. Four selected periods are shown: 1) prevailing southwesterly wind, 1–21 March; 2 and 3) prevailing northerly wind, 27 May–4 June and 10–25 June; 4) prevailing southwesterly wind, 2 July–10 July. The green dotted line marks the beginning and red dashed line marks the end of the period. Wind data were smoothed with a 36-h filter. Color scale shows wind speed in m s^{-1}.

381

382
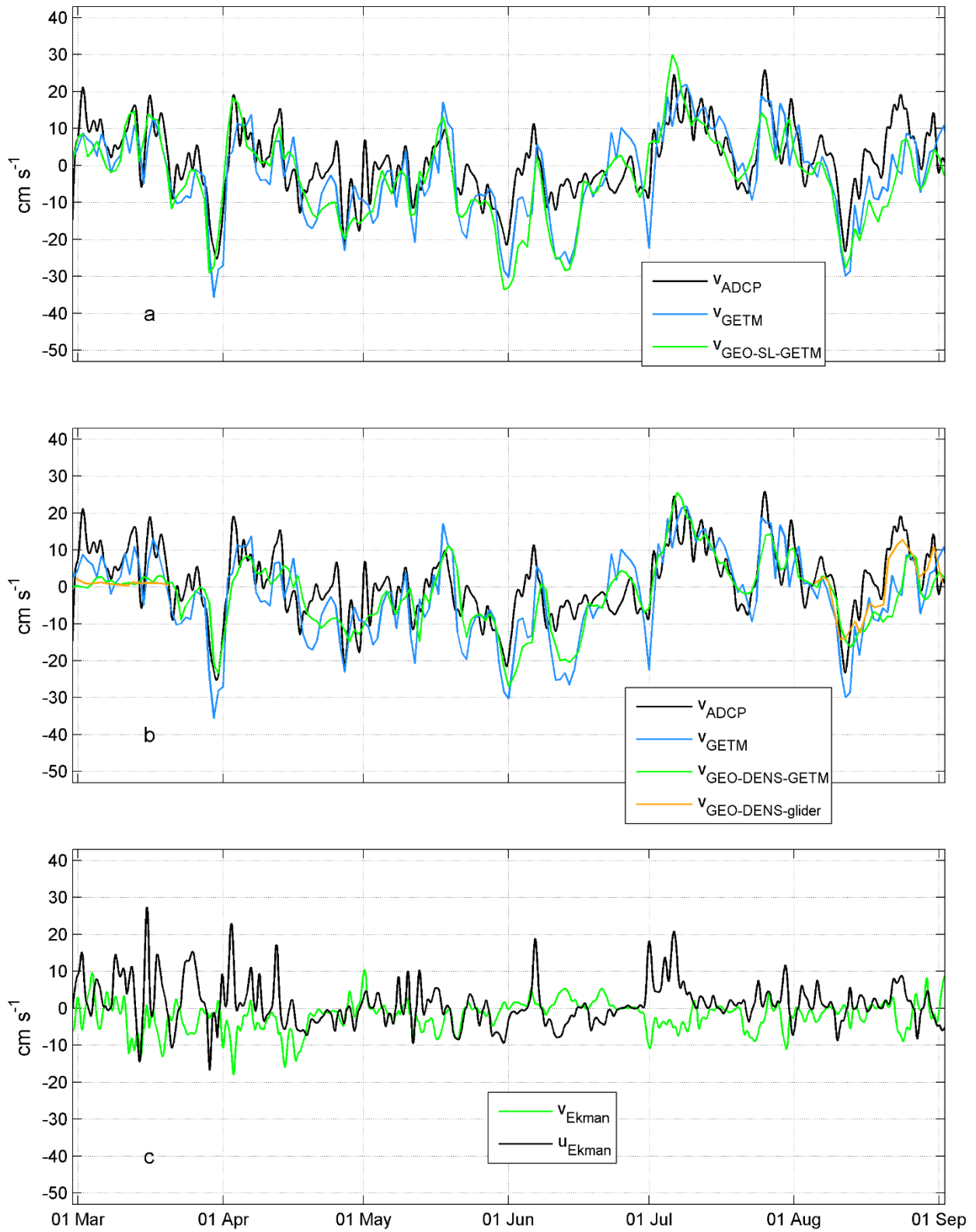
Figure 5. Temporal courses of (a and b) current velocity *v*-component (positive northward) measured by ADCP (V_{ADCP}), simulated *v*-component (V_{GETM}), estimated from the GETM sea level data ($V_{GEO\text{-}SL\text{-}GETM}$), estimated from temperature and salinity data collected by glider ($V_{GEO\text{-}DENS\text{-}glider}$), estimated from temperature and salinity data simulated by GETM at 11 m depth ($V_{GEO\text{-}DENS\text{-}GETM}$). Mean Ekman current *u*-component (positive eastward) and *v*-component (U_{Ekman} and V_{Ekman}) in the depth range 0–11 m (c). Time-series are shown from March to September 2020 at the ADCP location (see Fig. 1b and c).
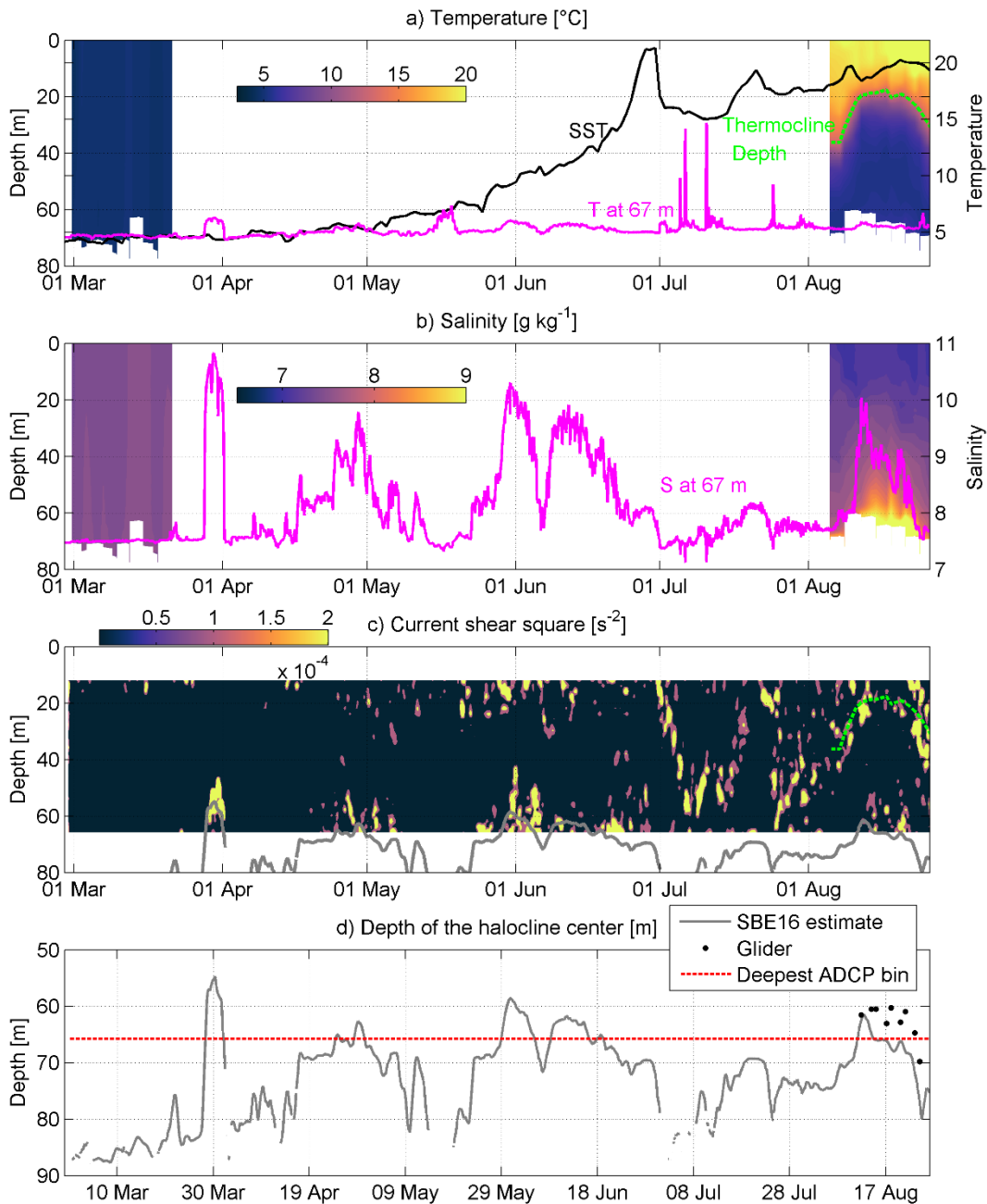
Figure 6. Temporal courses of temperature, salinity, current shear squared and halocline depth in the ADCP location from March to September 2020 (see Fig. 1b and c). (a) Temporal course of sea surface temperature

393 (SST) and temperature at 67 m depth; temporal course of the vertical distribution of mean temperature in March
394 and August calculated from glider data (color scale). Depth of the thermocline center is shown as red dashed
395 line. (b) Temporal course of salinity at 67 m depth; temporal course of the vertical distribution of mean salinity
396 in March and August calculated from glider data (color scale). Mean temperature and salinity profiles were
397 calculated for each glider passing within the 3.7 km zonal window around the ADCP location. Depth of the
398 thermocline center is shown as red dashed line. (c) Temporal course of the vertical distribution of current shear
399 squared and depth of the halocline center (grey line). (d) Depth of halocline center, calculated from SBE16 data
400 and in August from glider data. Depth of deepest ADCP bin is also shown (red dotted line).

401 **3.2 Quasi-permanent circulation patterns**

402 In the previous chapter, we demonstrated the importance of wind forcing and stratification for the
403 currents. Next, we describe the current structure during the quasi-steady forcing periods. We have
404 selected four periods of 8–21 days duration with relatively stable forcing (see Fig. 4) to analyze the
405 mean measured and simulated flow structure in the ADCP and Valeport locations (Fig. 7) and along
406 the zonal section (Fig. 8). Likewise, we investigated the horizontal structure of simulated flow in the
407 three forcing cases in three layers: upper layer (5 m), intermediate layer (40 m) and deep layer (110 m)
408 (Figs. 9–11).

409 The persistency of the measured currents in the ADCP location was very high in all selected periods
410 (Table 2). Only during the fourth period, the persistency was lower than 50% below the seasonal
411 thermocline. Particularly high persistency (82–94%) occurred in the first and second periods. Thus,
412 measured currents during the quasi-steady forcing have much higher persistency than overall of the
413 time series (see Table 1).

414 Barotropic flow to the northeast prevailed throughout the water column at the ADCP location in the
415 first period (1–21 March) when south-westerly wind prevailed (Fig. 7a, b and c). Even stronger mean
416 current to the north-northwest was registered at 5 m depth at the Valeport location (Fig. 7b). Latter
417 indicates the boundary effect near the Saaremaa Island, the current was directed along the coast (Fig.
418 1c). Mean flow was to the south in the upper layer (Fig. 7g) during the second period (27 May–4 June)
419 when northerly wind prevailed (Fig. 7e), to the southeast below the thermocline and to the east below
420 the halocline (Fig. 7f and g). In general, a similar current pattern occurred in the third period (10–25
421 June) when north-westerly wind prevailed (Fig. 7i, j and k). Due to relatively strong south-westerly
422 wind forcing in the fourth period (2–10 July), flow to the northeast prevailed in the upper layer and to
423 westerly directions below the thermocline (Fig. 7m and n).

424 In conclusion, a pattern typical for the downwelling event – current to the northeast along the boundary
425 and towards the shore in the upper layer (Fig. 7n and o) and seaward current to the southeast in the
426 deep layer (Fig. 7n) occurred during southwesterly wind domination (Fig. 7m). On the contrary, a
427 pattern typical for the upwelling: the flow was to the south along the coast in the upper layer (Fig. 7g
428 and k) and onshore (east) in the deeper layers (Fig. 7f, j, g and k) were observed in the case of northerly
429 winds (Fig. 7e). These vertical patterns (downwelling and upwelling) of the current velocity were also
430 well captured by the numerical model. The stronger mean measured current at 5 m depth near the
431 boundary (Valeport location), was well reproduced by the model (Fig. 7b and c). The mean adjusted
432 geostrophic velocity profiles based on simulation data had a quite similar vertical structure compared
433 to the measured mean velocity profiles in all periods (Fig. 7, second and fourth columns). Thus,
434 currents were generally in geostrophic balance during the quasi-steady periods. The transition from
435 one state to another has likely an ageostrophic nature, as wind is the main driver for the change.

436 Next, to understand the larger scale circulation dynamics during the periods, we analyze the vertical
437 structure of the mean meridional component of currents (Fig. 8) in the section along the latitude of the
438 ADCP location (Fig. 1b) and the horizontal structure of mean currents at selected depths (Figs. 9–11)
439 in the Eastern Gotland Basin (Fig. 1b) using simulated current data. The current data are averaged
440 within the same time windows with relatively stable wind forcing as analyzed above.

441 The structure of the meridional component of currents in the section is characterized by high spatial
442 and temporal variability (Fig. 8). The unidirectional flow prevailed in most of the section down to the
443 halocline or even deeper in the case of no thermal stratification and southwesterly winds (first period)
444 (Fig. 8a). The northward current along the eastern boundary with a cross-coast extent of 10 km was
445 especially strong. This strong boundary current was also registered by the Valeport (Fig. 3d). The
446 strong maxima of the northward flow can be found between 20.5°–21.0° E, 18.6°–19.3° E and around
447 17.6° E. The strong southward flow prevailed between 21.0°–21.3° E, 19.4°–20.0° E, and 17.6°–18.6°
448 E. Horizontal flow structure in the Eastern Gotland Basin consisted of the two stronger current zones
449 above the halocline (at a depths of 5 and 40 m), northward current along the eastern bottom slope and
450 southward current along the bottom slope in the western part of study area (Fig. 9a and b). The two
451 zones were connected with several cyclonic cells. The northward flow below the halocline at a depth
452 of 110 m (Fig. 9c) coincided with the flow in the upper layer along the bottom slope in the Eastern
453 Gotland Basin area but was forced to the westward trajectory by bathymetry in the northern area.

454 The mean meridional current patterns were very similar in the following two periods (second and third)
455 of prevailing northerly winds and the presence of thermocline. In both cases, the zonal scale of the
456 southward flow around the ADCP location was 10–15 km (Fig. 8b and c). The flow did not extend to
457 the eastern boundary, a narrow northward flow with a width of 5–10 km occurred along the coastal
458 slope. The width of the southward flow near the western boundary of the section was about 30 km. In
459 between, several circulation cells with zonal scales of 20–60 km can be distinguished in the cross-
460 section (Fig. 10a). The horizontal structure of the flow below the thermocline at a 40 m depth in the
461 Eastern Gotland Basin revealed a strong southward current in the eastern part of the area in the second
462 period (Fig. 10b). The current swirled, split into two branches and re-merged back to one in several
463 locations. The southward flow below the thermocline (40 m depth) coincided with the offshore branch
464 in the upper layer in the central area of the basin (Fig. 10a and b). Sub-halocline flow revealed strongest
465 northward current along the bottom slope and strongest cyclonic cell in the Eastern Gotland basin
466 among the selected periods (Fig. 10c).

467 The flow pattern in the case of strong southwesterlies dominance (fourth period) under stratified
468 conditions revealed a strong northward current component along both boundaries of the section (Fig.
469 8d). In between, the strong southward flow occurred in the surface layer. Similarly, to the northerly
470 wind prevailing, complicated three-layer structure with variable horizontal patterns in the zonal scale
471 of 20–60 km occurred. Flow to the southeast prevailed for most of the study area in the upper layer (5
472 m depth), except in the eastern boundary zone, where a strong northeastward downwelling related flow
473 occurred (Fig. 11a), as also was observed in our ADCP mooring data (Fig. 7n). A strong current
474 occurred also in the Irbe Strait towards the Gulf of Riga. Downwelling related flow along the eastern
475 coast was also observed at 40 m depth (Fig. 11b). In the deep layer below the halocline (110 m depth),
476 northward current along the eastern bottom slope and cyclonic cells in the Eastern Gotland Basin were
477 observed (Fig. 11c).

478

479   Due to seasonality in forcing, variations in the circulation in this time scale can be expected. Next, we
480   analyze the vertical distribution of monthly mean (April, July and December) and annual mean
481   meridional velocity component (Fig. 12) along the zonal section (Fig. 11) at ADCP latitude based on
482   simulation data from September 2010 to August 2020. The boundary current along the eastern coastal
483   slope occurred year-round (Fig. 12d) but was the strongest in winter (Fig. 12c). This is related to the
484   wind regime: southwesterly winds prevail more in winter but are less frequent in spring and summer.
485   The seasonal signal can be found in the whole section (Fig. 12a, b and c). Well defined large cyclonic
486   gyres in the Northern Baltic Proper can be found in winter (Fig. 12c), while in spring and summer (Fig.
487   12a and b), the mean current structure is characterized by the smaller scale zonal features and weaker
488   flow. However, it is noteworthy that the mean flow is to the north along the eastern coastal slope in all
489   seasons.

490

491   **3.3 Sub-halocline current**

492   As shown above, cyclonic gyre was present below the halocline in the Eastern Gotland Basin in all
493   selected periods (Figs. 9–11). The flow in this cyclonic system was especially strong along the eastern
494   slope of the Eastern Gotland Basin. The northern branch of this circulation system is connected to the
495   clearly distinguishable northward current. The position and magnitude of the current varied under
496   different conditions. The current was stronger and meandered to west at the shallower area between
497   Gotland and Fårö Deep in the case of northerly wind while it was slower, and the meandering did not
498   occur in the case of southwesterly winds. To confirm the simulated cyclonic circulation in the Eastern
499   Gotland Basin and the northward flowing current towards the Northern Deep, the Argo float trajectory
500   and the mean current field between 105–135 m depth were plotted in the same time frame from 15
501   August 2013 to 15 August 2014 (Fig. 13a). The general features in the simulated mean currents and
502   the Argo float trajectory agreed well. The Argo float first completed two circles (smaller and larger) in
503   the Eastern Gotland Basin and then headed to the north. The float arrived and was recovered in the
504   shallower area between the Fårö and Nothern Deep. This sill is an important location for the deep layer
505   water renewal in the Northern Baltic Proper, as this is the only remarkable passage to the north below
506   100 m depth (see bathymetry in Fig. 1b). The sill is located slightly south of the selected section along
507   the latitude of the ADCP deployment.

508   The mean simulated meridional flow to the north over the still was concentrated in a narrow cell with
509   a zonal scale of 5–6 km in 2010–2020 (Fig. 14a). The flow was especially strong when northerly winds
510   prevailed, e.g., in the second period from 27 May to 4 June 2020 (Fig. 14b). The mean density field
511   sloped downward in the left (west) of the flow (Fig. 14a and b), typical for a gravity current. The
512   meridional current velocity (C_T) in the trench was mostly positive (northward) and in the range of 10–
513   20 cm s^{-1} during the study period March–September 2020 (Fig. 14c). The C_T was reversed in the first
514   half of July, which coincided with the strong southwesterly wind impulse (Fig. 4). The time series of
515   C_T for 2010–2020 (Fig. 14d) revealed many reversal events, but the long-term mean meridional
516   velocity was 10 cm s^{-1} to the north. Reversals were most frequent in November–December when the
517   monthly mean southward C_T was 6–7 cm s^{-1} and rarer in March–May when monthly averages were in
518   the range of 12–14 cm s^{-1}. Thus, the deep layer water renewal in the Northern Baltic Proper is most
519   active in the spring period and more restricted in late autumn–early winter. The best correlation
520   (r^2=0.25, p<10^{-100}, n=3838) between 10-day low-pass current velocity at the sill and wind was found
521   with the wind from ENE (70°) with a delay of 6 days. This is another confirmation that prevailing
522   southwesterly winds slow down or reverse the C_T and prevent deep water renewal in the Northern
523   Baltic Proper.

524

525 **Table 2.** Persistency (%) of the measured currents in the ADCP location at the selected depths during the
526 selected periods: 1 March to 21 March (1); 27 May to 4 June (2); 10 June to 25 June (3); 2 July to 10 July (4)
527 in 2020.

Period/ depth (m)	1	2	3	4
10.8	84.8	82	75.8	83.1
20.8	88.8	92.3	76.9	78.9
30.8	88.8	94	66.2	54.8
40.8	88.6	92.5	62.1	41.3
50.8	89.3	89.9	61.4	24
60.8	87.7	91.1	70.1	27.5
66.8	87.2	86.1	64.1	4.7

528
529
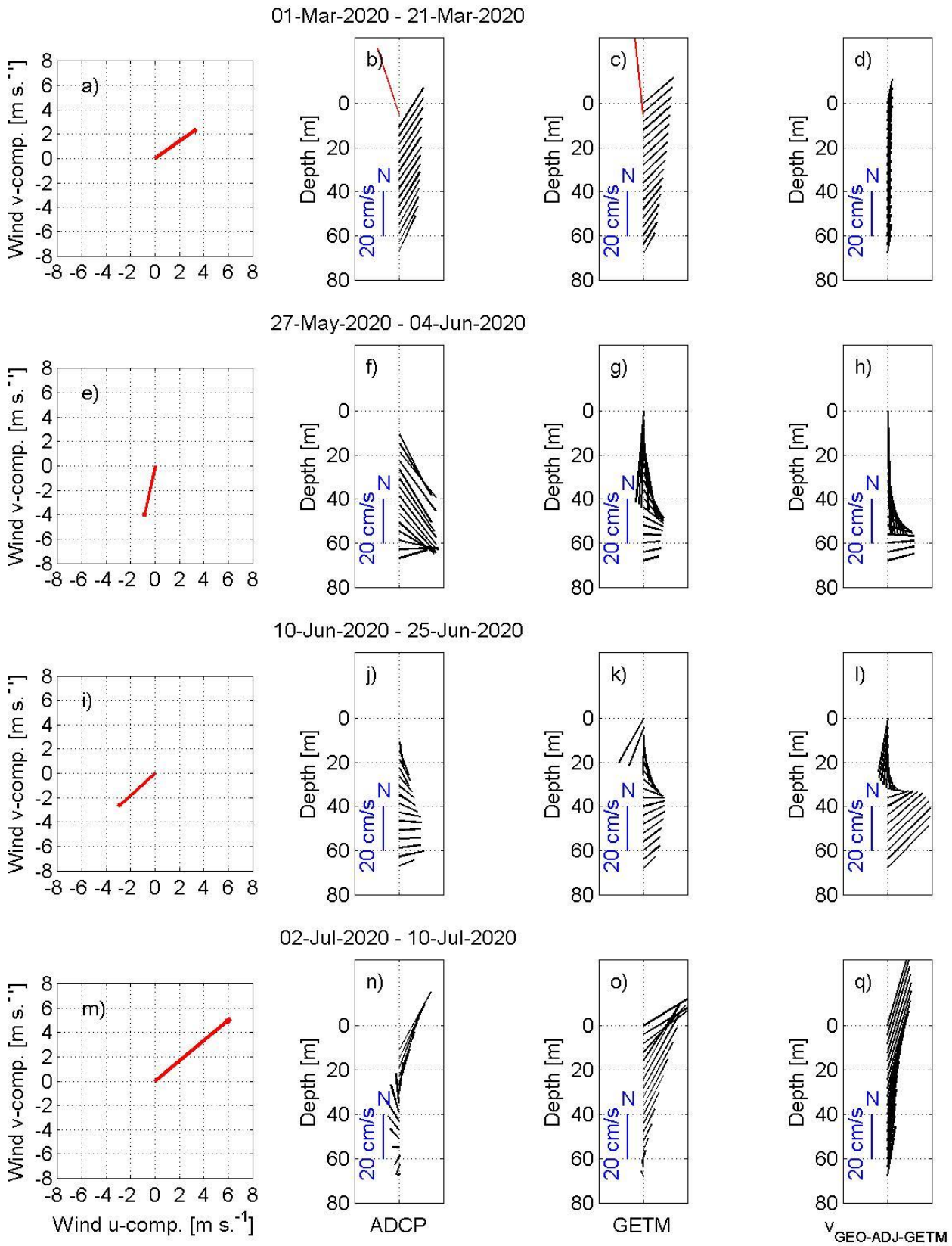
530
531   **Figure 7.** The mean resultant wind vectors (a, e, i, m), mean profiles of current velocity vectors calculated from
532   ADCP data (black arrows, b, f, j, n) and mean simulated current velocity vectors at the ADCP location (c, g, k,

o) are shown for selected periods (Fig. 4). The mean current velocity vector at 5 m depth based on Valeport data (b, red arrow) and mean simulated current velocity vector at the Valeport location (c, red arrow) for the first time period are shown. On the right panels, mean adjusted geostrophic velocity vectors $V_{GEO\text{-}ADJ\text{-}GETM}$ (d, h, i, q) are shown.
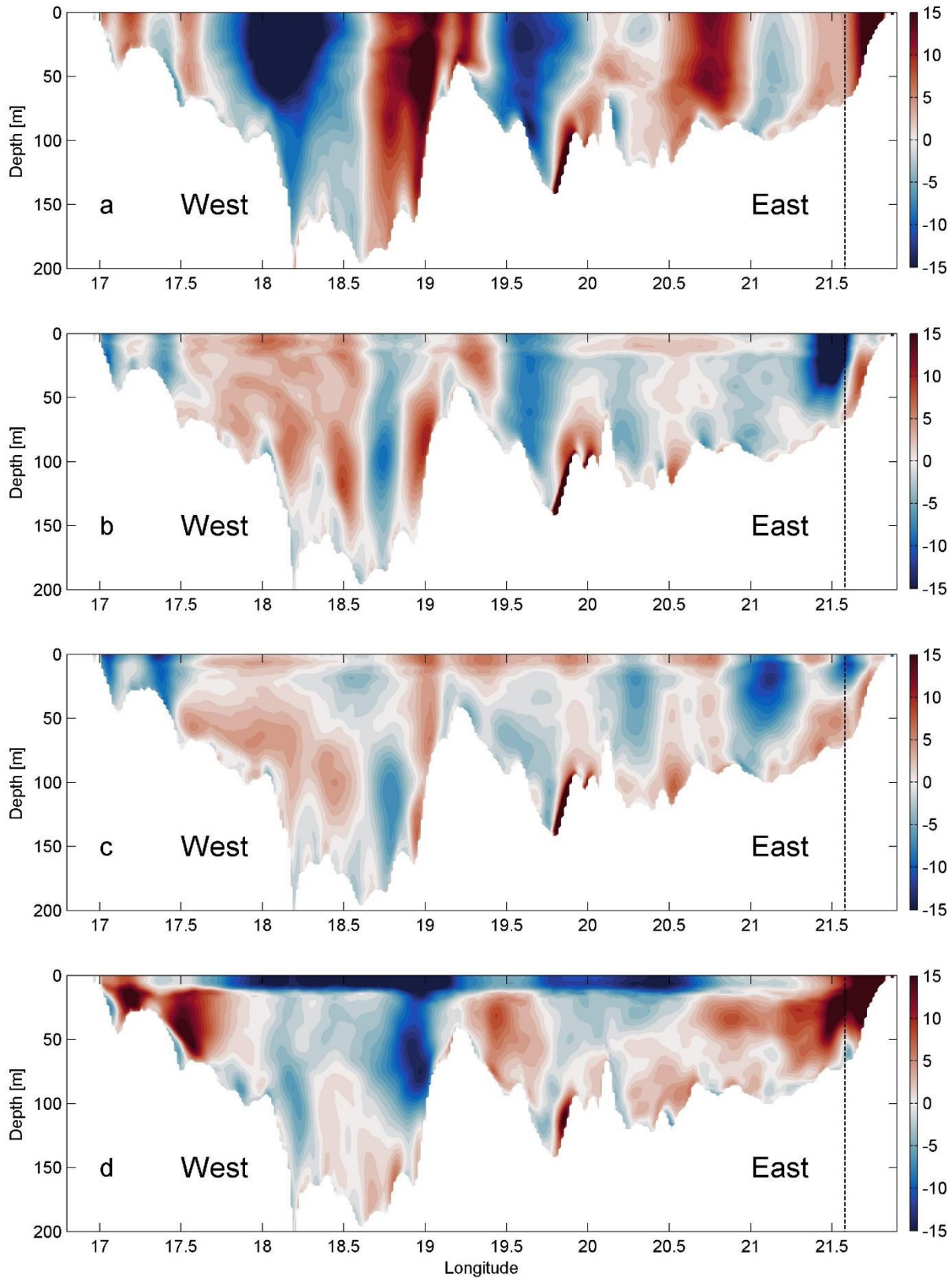
538   **Figure 8.** Vertical distribution of simulated mean meridional current velocities for four selected periods: a) 1–
539   21 March, b) 27 May–4 June, c) 10–25 June and d) 2 July–10 July 2020 (see Fig. 4) along the ADCP deployment
540   latitude (Fig. 1b). Color scale displays meridional velocity (positive northward) in cm s^{-1}. Vertical dotted lines
541   show the ADCP location.
542
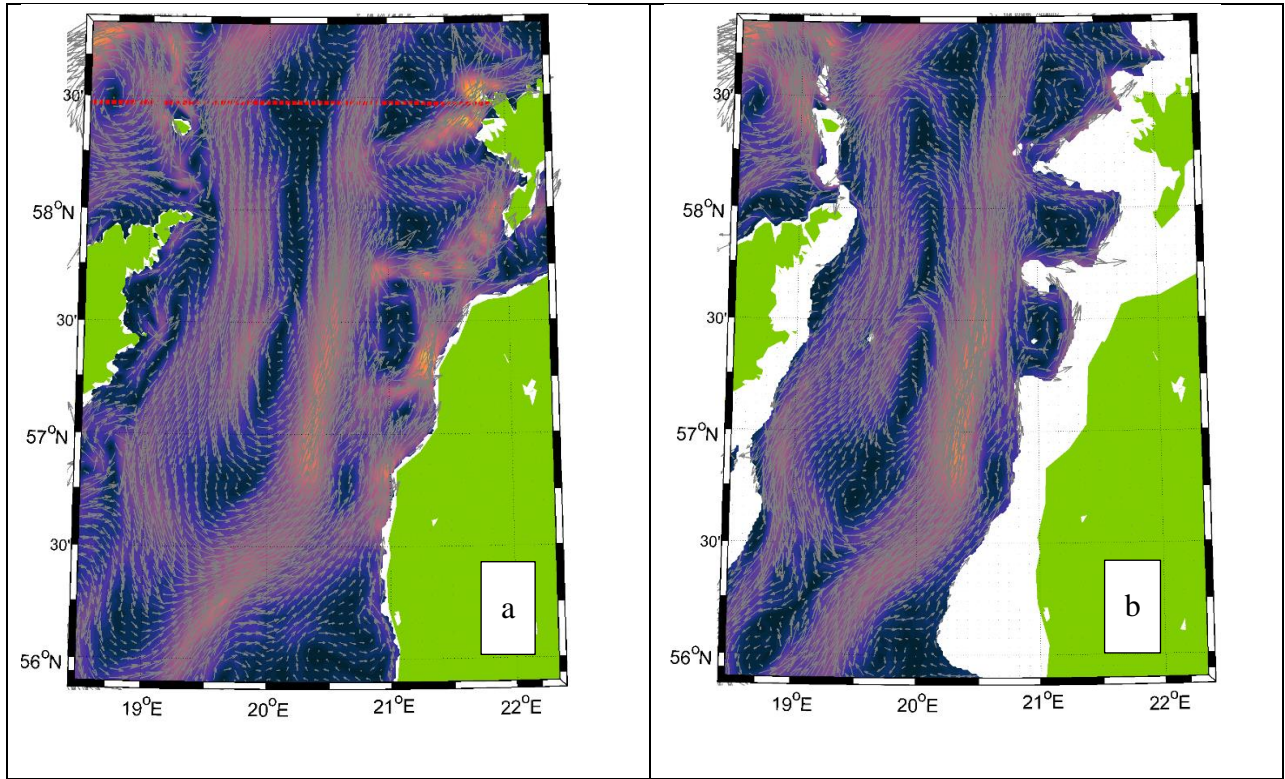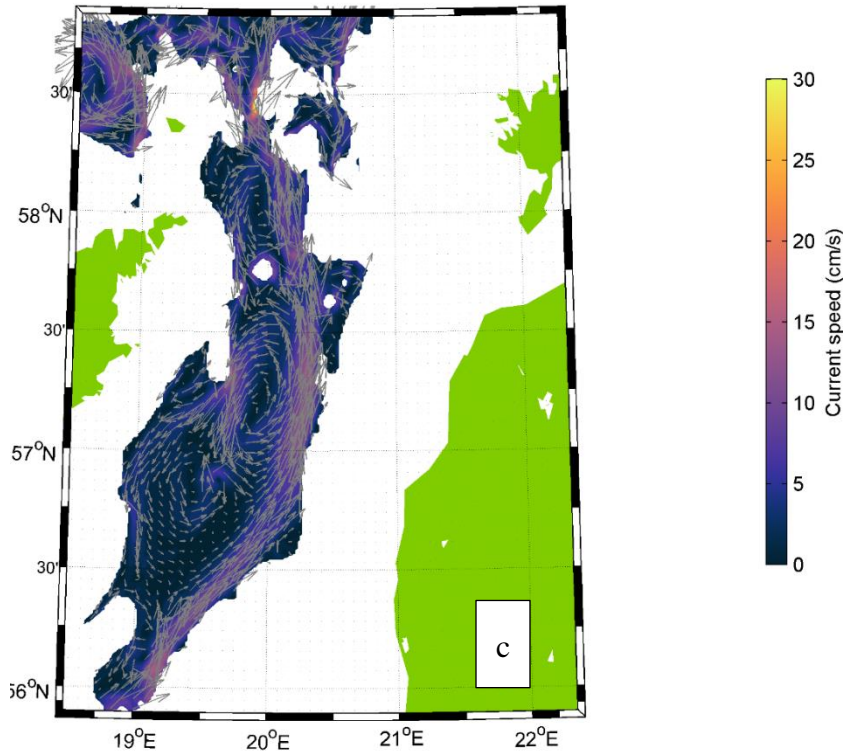
543
544 **Figure 9.** Mean simulated currents in the case of prevailing south-westerly winds from 1 March to 21 March
545 2020, without thermocline at 5 m depth (a), 40 m depth (b) and 110 m depth (c). Color scale shows current speed
546 in cm s⁻¹. Red dashed line on panel (a) shows the location of the transect presented in Figs. 8 and 12.
547

548
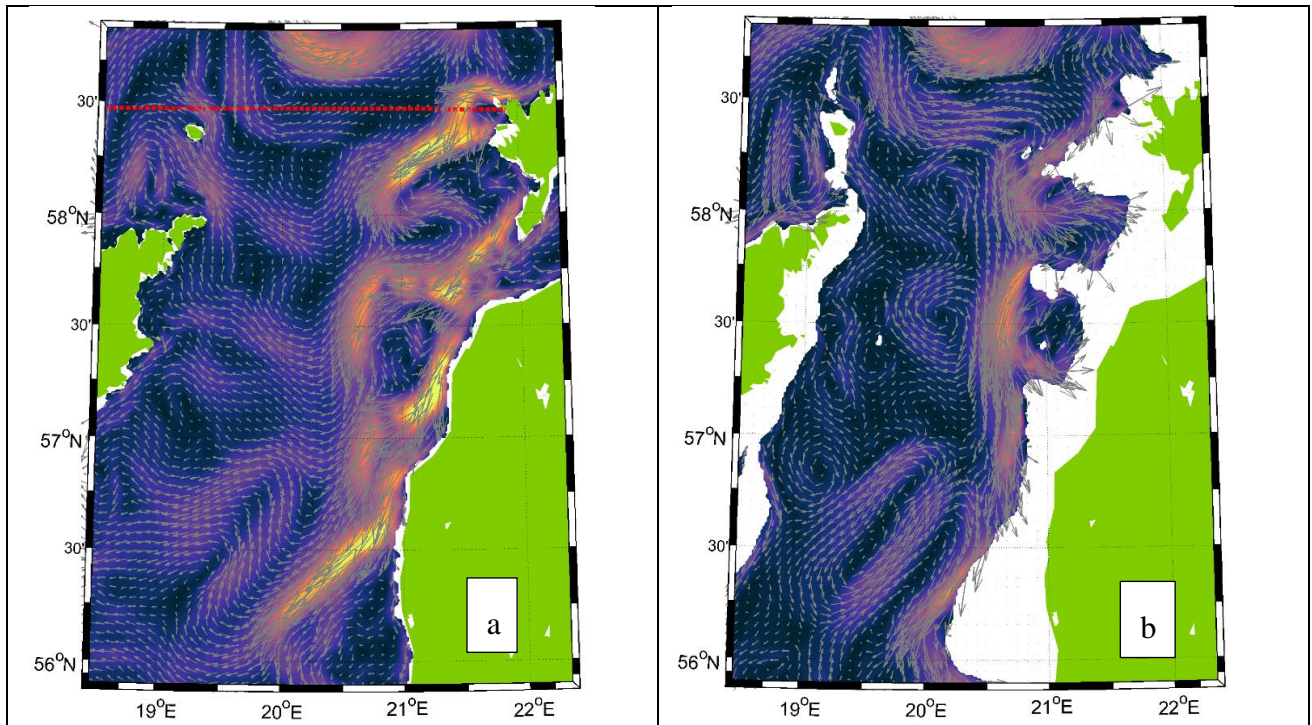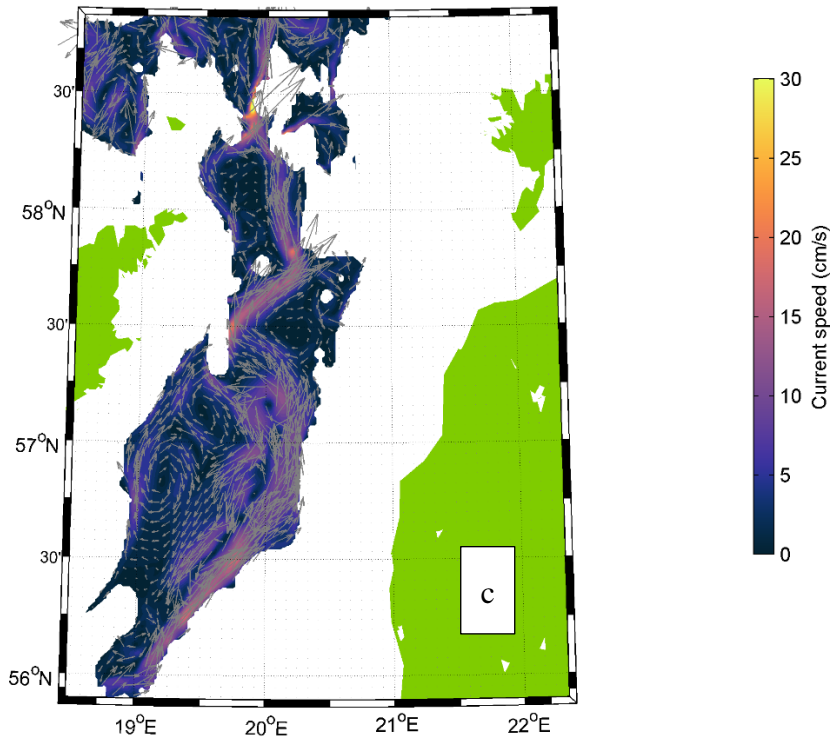
549
550
551
552 **Figure 10.** Mean simulated currents in the case of prevailing northerly winds from 27 May to 4 June 2020, with
553 thermocline at 5 m depth (a), 40 m depth (b) and 110 m depth (c). Color scale shows current speed in cm s^{-1}.
554 Red dashed line on panel (a) shows the location of the transect presented in Figs. 8 and 12.
555
556
557
558
559
560
561
562
563
564
565
566
567

568
569 **Figure 11.** Mean simulated currents in the case of prevailing south-westerly winds from 2 July to 7 July 2020,
570 with thermocline at 5 m depth (a), 40 m depth (b) and 110 m depth (c). Color scale shows current speed in cm
571 s⁻¹. Red dashed line on panel (a) shows the location of the transect presented in Figs. 8 and 12.
572
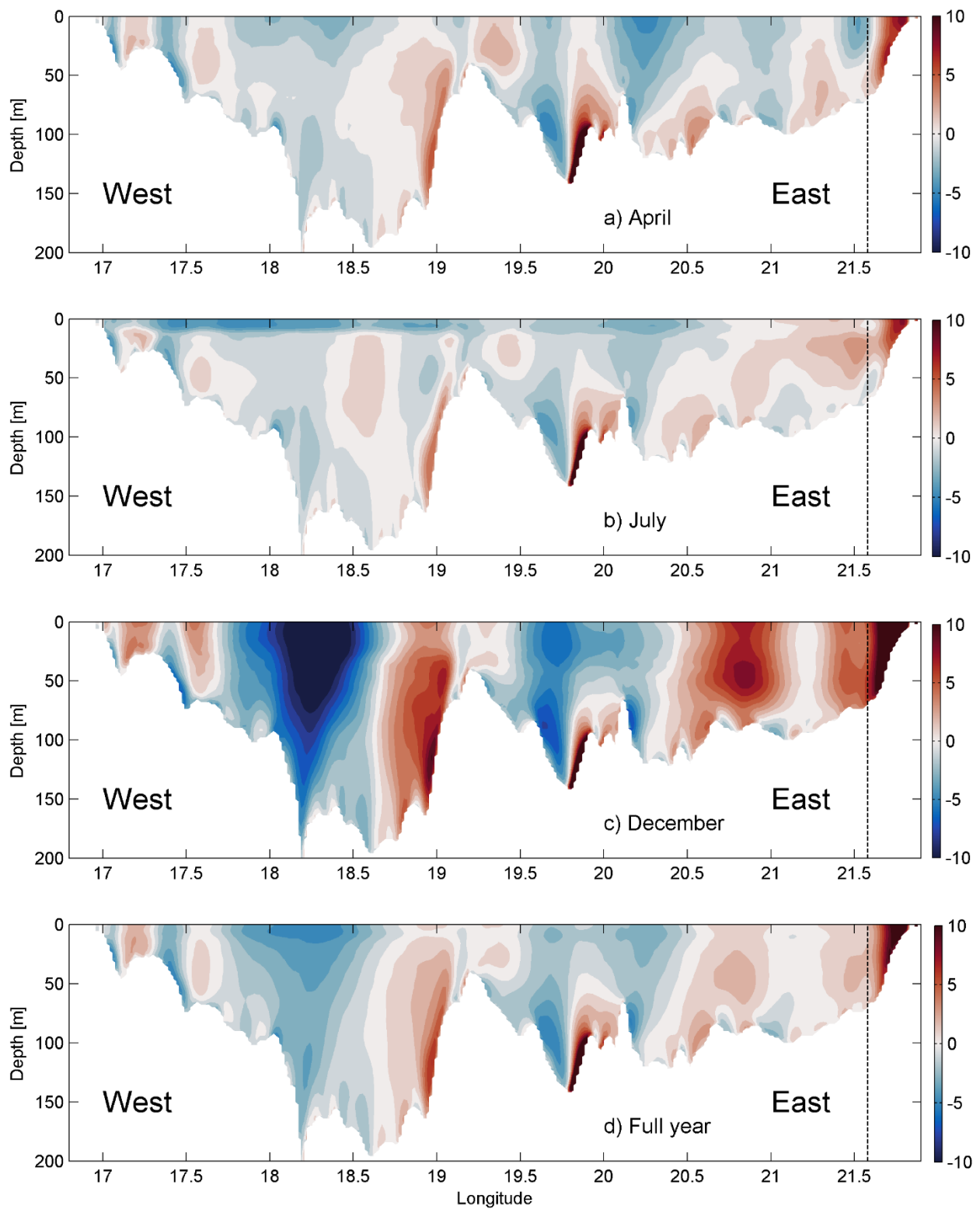
573
574 **Figure 12.** Vertical distribution of monthly mean (April, July and December) and annual mean meridional
575 velocities (positive northward) along the zonal section at ADCP latitude based on simulation data from

576 September 2010 to August 2020. Color scale shows meridional velocity in cm s⁻¹. Vertical dotted lines show
577 the ADCP location.
578
579
580
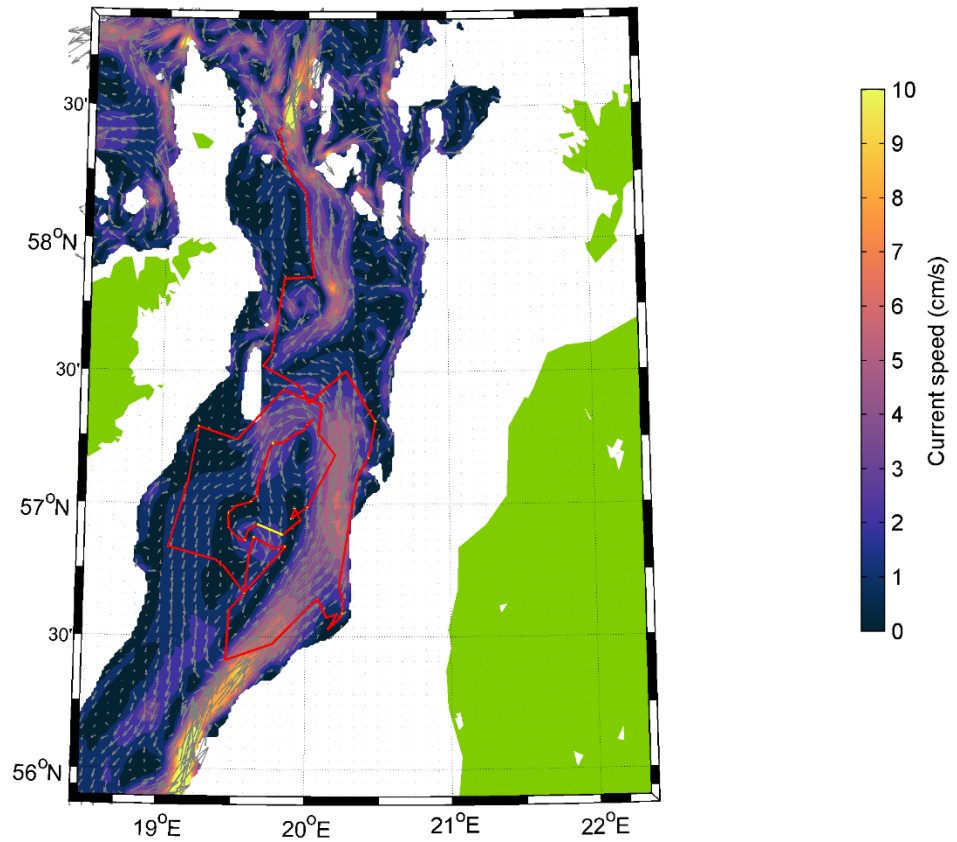
581
582 **Figure 13.** Mean current field between 105–135 m depth based on simulation data and ARGO (WMO number
583 6902014) float trajectory during the period 15 August 2013–15 August 2014 in the deep layer (within its parking
584 depth range 105–135 m, shown in red). Only one longer period occurred, when the float drifted on the surface
585 (shown in white). Color scale shows current speed in cm s⁻¹.
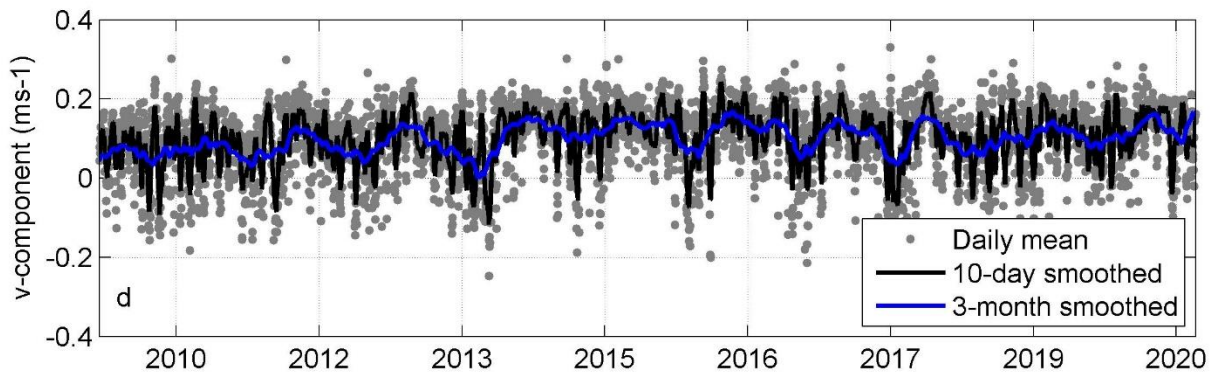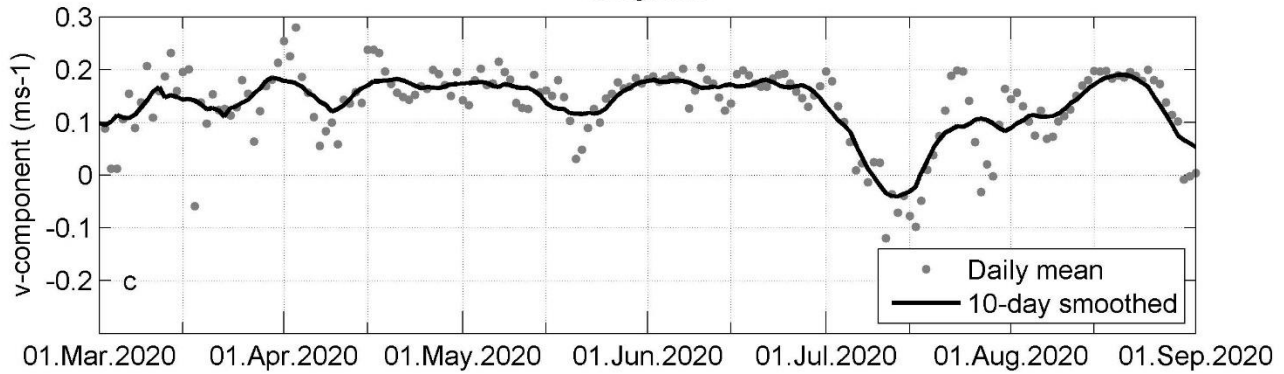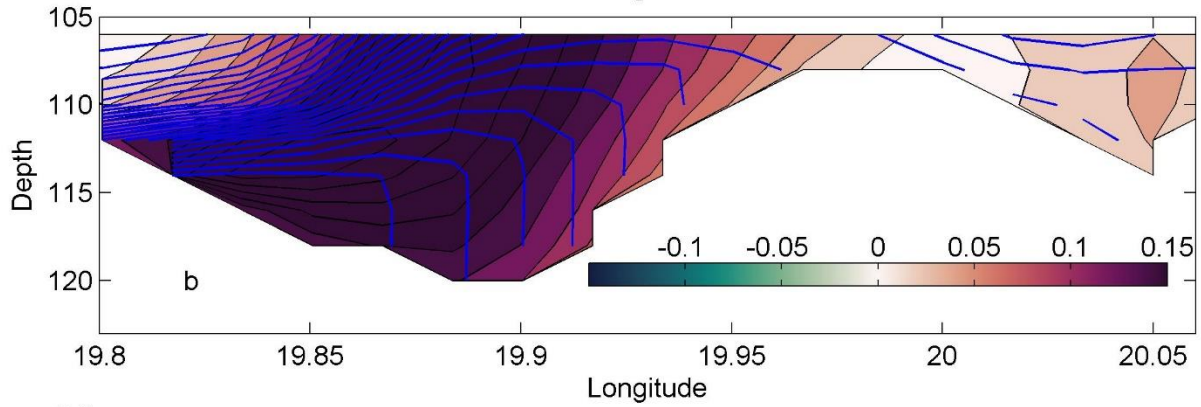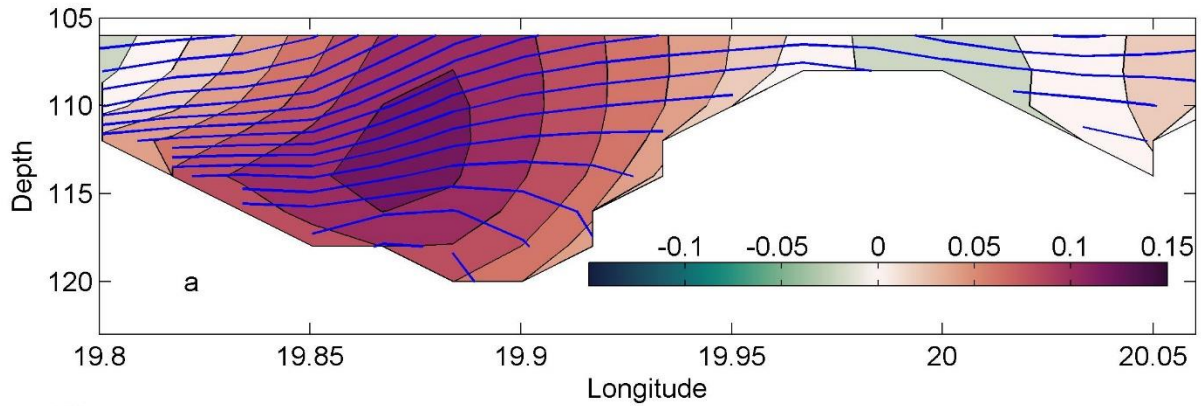
586
587 **Figure 14.** (a) mean simulated meridional current component *v* (positive northward) and density isolines at
588 section below 105 m depth (the section location is shown as red line in Fig. 1b) in 2010–2020, (b) mean

589 simulated meridional current component *v* and density isolines at section below 105 m depth from 27 May to 4
590 June 2020 during a northerly wind impulse. In color scale contours with step of 2 cm s^{-1} show current *v*-
591 component (m s^{-1}, positive northward) and blue lines show density isolines with a step of 0.05 kg m^{-3}. (c) time-
592 series of *v* component below 105 m at the sill. Dots marks the daily mean and bold line 10-day smoothed *v*-
593 component from March to September. (d) time-series of *v* component below 105 m at the sill. Dots marks the
594 daily mean, bold black line 10-day smoothed and bold blue line 3-month smoothed *v*-component in the period
595 2010–2020.
596
597

4 Discussion

599 Moorings carrying ADCP and single-point current meter, and underwater glider surveys were applied,
600 together with numerical modeling to investigate circulation in the Baltic Proper.

601 Strong linkage between the vertical location of the current shear maxima and the two pycnoclines was
602 observed. The same finding was reported in the Gulf of Finland (Suhhova et al., 2018). The current
603 shear maxima in the Gulf of Finland were related to the along-gulf estuarine circulation and its
604 alterations. In the present case, the shear maxima were related to the currents along the basin axis and
605 the coastal downwelling and upwelling circulation structures. The separation of the cross-shelf flow
606 by a pycnocline has been documented in several other coastal systems (Davis, 2010; Gilcoto et al.,
607 2017; Villacieros-Robineau et al., 2013).

608 Boundary current in the upper layer along the eastern coast was observed. The current was well
609 correlated with the wind. The wind regime in the area is the combination of the global circulation and
610 specific direction-dependent boundary-layer effects, which results in domination of winds along the
611 axis of the Baltic Proper (Soomere & Keevallik, 2001). Along-axis wind causes the Ekman current
612 (Ekman, 1905) to the right from wind direction in the upper layer, i.e., a flow across the basin axis.
613 The resulting convergence (divergence) in the case of southwesterly (northerly) winds at the eastern
614 coast causes across-axis sea level gradient and the upper pycnocline inclination, which in turn cause
615 horizontal pressure gradient, and results in a geostrophic flow to the north (south) in the upper layer.
616 Boundary currents forced by the pressure gradient caused by wind-driven divergence/convergence are
617 common in coastal systems (Berden et al., 2020; Longdill et al., 2008; H. Wu et al., 2013). The
618 geostrophic current velocity is well agreed with the total current velocity profiles. Thus, the current
619 along the boundary was generally in the geostrophic balance, but across-shore ageostrophic flow
620 created preconditions for this geostrophic coastal current.

621 Circulation rapidly reacted to the wind forcing. Persistency of the current for 6 months was rather low
622 (30–40%) due to variability in the wind forcing. The estimated persistency from long-term numerical
623 simulations data in the same area above the halocline was 70–80% in 1981–2004 (Meier, 2007) but
624 around 30–40% in the upper layer in 1958–2007 (Jędrasik & Kowalewski, 2019). However, the quasi-
625 steady circulation patterns detected under different wind and stratification conditions were high-
626 persistent, mostly >75%.

627 The mean cyclonic circulation in the upper layer of the Baltic Proper has been reported by many
628 modeling studies (Hinrichsen et al., 2018; Jedrasik et al., 2008; Jędrasik & Kowalewski, 2019; Meier,
629 2007; Placke et al., 2018). However, the magnitude of the long-term mean circulation patterns had a
630 considerably lower magnitude than the quasi-steady circulation structures presented in this study.
631 Likewise, the current direction of quasi-steady patterns varied and differed considerably from the long-
632 term mean. The circulation structures in this timescale also differ from the long-term mean because of

633 seasonal and inter-annual variations in the forcing. The cyclonic circulation and the eastern boundary
634 current towards the north in the upper layer is stronger in autumn and winter, as noted by previous
635 simulations (Jędrasik & Kowalewski, 2019), when strong southwesterly winds are more frequent
636 (Soomere & Keevallik, 2001). Quasi-steady circulation patterns were characterized by complicated
637 lateral vortices with the zonal scale of 20–60 km. The richness of vortical structures has been suggested
638 by several numerical modeling studies (Dargahi, 2019; Zhurbas et al., 2021). In-situ measurements are
639 needed to verify the existence of the vortices and to characterize their effect on the physical and
640 biogeochemical fields in more detail.

641 Two quasi-permanent circulation features were detected in the deep layer. Cyclonic gyre was present
642 below the halocline in the Eastern Gotland Basin, with the strongest flow along the eastern slope, which
643 has been documented by in-situ measurements earlier (Hagen & Feistel, 2004; Hagen & Feistel, 2007).
644 The northern branch of the Eastern Gotland Basin current is connected to the quasi-steady northward-
645 flowing current towards narrow Fårö sill between the Fårö and Nothern Deep. The width of the current
646 was mostly 10–30 km, but only 5 km at the sill. The mean northward component of the current was 10
647 cm s^{-1}, which can be explained by the mean density structure (Fig. 14a) and is typical for the gravity
648 current in a channel (Zhurbas et al., 2012). This current is an important deeper limb of the Baltic haline
649 conveyor belt (Döös et al., 2004). The current was stronger in the case of northerly winds and weaker
650 during southwesterly wind prevailing. This is typical behavior of the estuarine circulation: up-estuary
651 wind causes weakening or reversal of the deep layer current and down-estuary wind intensification of
652 the estuarine current (Geyer & MacCready, 2014) as observed in the Gulf of Finland (Liblik et al.,
653 2013; Lilover et al., 2017; Suhhova et al., 2018) and several other estuaries (e.g. Giddings &
654 MacCready, 2017; Scully, 2016). In the case of northerly wind, the vertical and horizontal density
655 gradient in the Fårö sill was much stronger (Fig. 14b) than the mean gradient in 2010–2020 (Fig. 14a)
656 according to the simulation. Note that on the right-hand flank, the isopycnals are vertical (Fig. 14b). A
657 similar structure of the gravity current has been measured by acoustic profiling in the Western Baltic
658 (Umlauf et al., 2009). The current to the north and potentially the deep layer water renewal in the
659 Northern Baltic Proper is more intense in March–May when southwesterly winds are less frequent, and
660 the current is weakest in November–December. If the water that overflows the Fårö sill is dense
661 enough, it occupies the Northern Deep bottom layers, and the old, oxygen-depleted bottom water is
662 lifted and advected to the Gulf of Finland, as observed during high Major Baltic Inflow activity (Liblik
663 et al., 2018). If the overflow has a lower density compared to the deep layer waters in the Northern
664 Deep, it does not dive to the bottom but stays as a buoyant layer.

665

666 The most favorable wind for the up-estuary deep layer advection in the Gulf of Finland is from the
667 northeast (Elken et al., 2003). Thus, northerly winds support deep water renewal and strengthening of
668 the stratification all the way from the Gotland Deep to the Gulf of Finland. The deep layer currents are
669 quite well covered by observations in the Gulf of Finland (Lilover et al., 2017; Rasmus et al., 2015;
670 Suhhova et al., 2018). However, observations are lacking from the Gotland Deep to the entrance of the
671 Gulf of Finland. The only in-situ record about the feature between Gotland and Northern Deep is the
672 Argo float track. The Argo trajectory supported our suggestion about the existence of the sub-halocline
673 current to the north. Our simulations suggested that the strength and position of the current did depend
674 on the wind forcing. Observations and simulation results at the channel-like topographic constriction,
675 Slupsk Furrow, in the southern Baltic have shown that the meandering of the gravity current is strongly
676 affected by the bottom topography and wind-forcing (Zhurbas et al., 2012). ADCP measurements are
677 needed to understand the behavior of the sub-halocline current better.

678 Overall, simulated currents quite well agree with the ADCP measurements in the upper layer. However,
679 the meridional component of the simulated current (V_{GETM}) was biased (Fig. 5a). The mean V_{ADCP} was
680 1.1 cm s^{-1}, but the mean V_{GETM} was –3.2 cm s^{-1} at 10 m depth during the study period. Such bias could
681 not be found in the deep layer. Flow to the north was often weaker compared to measurements (V_{ADCP}),
682 and flow to the south was stronger than observed by the ADCP in the upper layer. A similar tendency
683 can be found in a comparison of the ADCP measurements and simulation results in the Gulf of Finland
684 (Suhhova et al., 2015). Near the right-hand side coast (looking up-estuary, i.e., to the east in the Gulf
685 of Finland), the down-estuary flow was stronger and more frequent in the simulation compared to the
686 measurements (see their Fig. 2). Interestingly, a similar bias was detected in the deep layer at the eastern
687 flank of the Gotland Deep at 204 m depth (Placke et al., 2018). Four different models considerably
688 underestimated (Placke et al., 2018) the mean flow to the north derived from observations (Hagen &
689 Feistel, 2004). The first possible explanation for the bias could be the smaller width of the boundary
690 current. Indeed, the mean flow towards north in 2010–2020 was stronger in the east from the ADCP
691 location (Fig. 12). The second possible source for the discrepancy could be related to the performance
692 of simulation of ageostrophic or geostrophic flow. We will discuss this further in the next section.

693 Quite large discrepancies between the simulation and the measurements occurred in June. In the first
694 half of the month, simulation was biased to the south, but in the second half, a bias to the north can be
695 seen (Fig. 5a). In both cases, the geostrophic current seems to play an important role in the discrepancy.
696 Strong simulated $V_{GEO-DENS-GETM}$ to the south (north) occurred in the first (second) part of June. In
697 August, the simulation did not capture the strongest flow event to the north on 21–24 August (Fig. 5a).
698 At the same period, much lower values of the $V_{GEO-DENS-GETM}$ compared to the $V_{GEO-DENS-glider}$ can be
699 seen. These signs suggest, first, that the isopycnals in the model react to the forcing more rapidly than
700 in the sea. Secondly, there is a bias in the across/slope seasonal thermocline inclination. Likely, the
701 thermocline is tilted more towards the surface near the coast in the model than in the sea. We next
702 evaluate the measured (by glider) and simulated temperature, salinity and geostrophic velocity fields
703 on 11–12 August and on 22–23 August.

704 Surface layer geostrophic velocity in the simulation agrees well with the estimates from the glider data
705 on 11–12 August (Fig. 16a–b). Though, the glider observations reveal sharper thermocline inclination
706 than the simulation. Discrepancies in the temperature, density, and geostrophic current fields on 22–
707 23 August are much larger (Fig. 16c–d). Glider observations revealed the thermocline depressed down
708 near the coast, which is typical for a downwelling. The inclination in the thermocline caused strong
709 geostrophic flow to the north in the location of ADCP (Fig. 16c). Homogenous mixed layer reached
710 down to 22 m depth at the easternmost end of the section. Such an inclination, well defined
711 homogenous layer and geostrophic current to the north at the ADCP location was not revealed by the
712 simulation (Fig. 16c). Thus, we can conclude that the bias in the boundary current simulation could be
713 related to the inaccuracy of reproducing the temperature and salinity fields and the resulting
714 geostrophic component of currents. We are not going into further details of this problem here, as it is
715 out of the focus of the present work. However, conclusions of the simulation studies that have focused
716 on the long-term mean current fields in the upper layer, but did not validate simulations with direct
717 current observations, should be taken carefully, as the magnitude of the long-term residual current is
718 very small compared to the magnitude of the currents during the quasi-steady states. We suggest a
719 dedicated study involving numerous current profiling records should be conducted to track down the
720 causes of the discrepancies between observations and simulations.

721

722
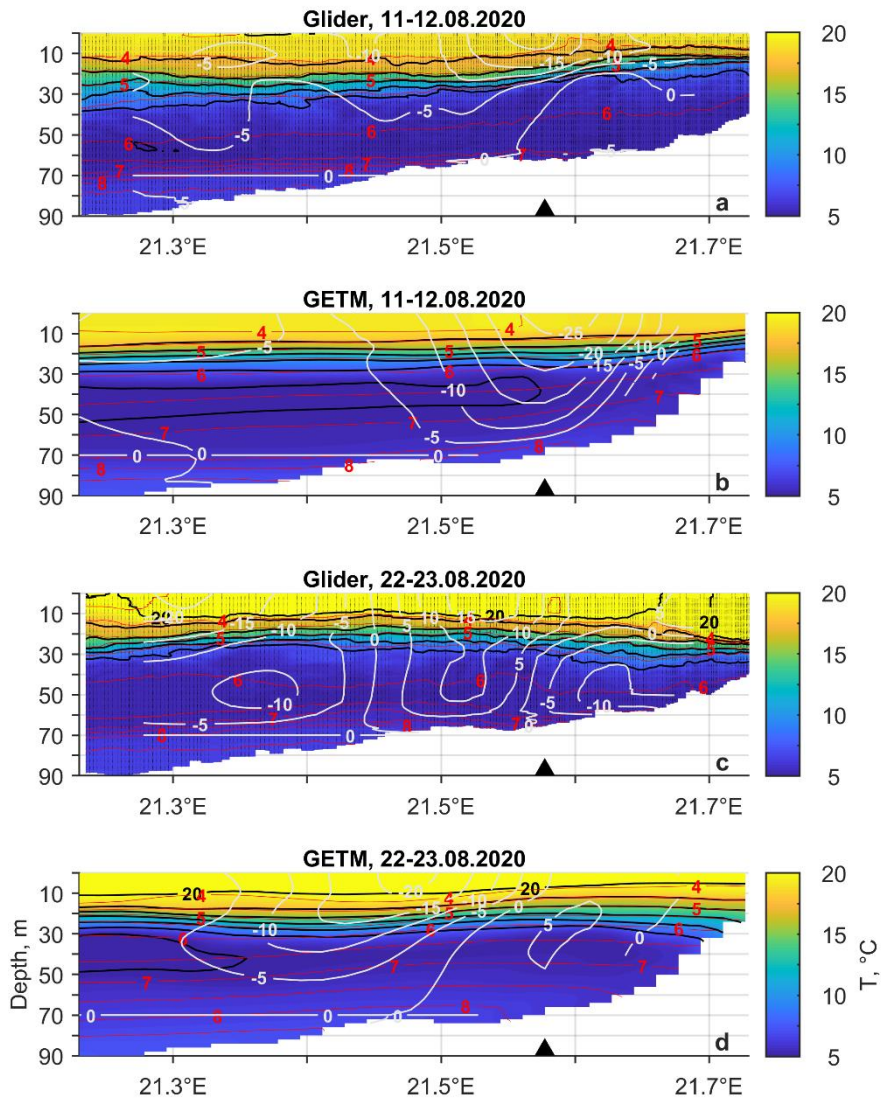
Figure 16. Temperature (color contours), density isolines (red lines), relative geostrophic current (white lines) based on glider observations and GETM simulation on 11–12 August and 22–23 August 2020.

725

726

727

5 Conclusions

A strong link between the existence and location of the two pycnoclines and the current structure was observed. Boundary current was observed in the upper layer along the eastern coast of the Baltic Proper. The current was mainly in geostrophic balance, and across-shore Ekman transport created preconditions for the geostrophic coastal current. The boundary current rapidly reacted to the changes in the wind forcing that was reflected in a relatively low persistency of currents (30–40%) in the whole water column during the 6-month measurement period. However, the quasi-steady circulation patterns formed under the certain wind and stratification conditions were high-persistent (mostly >80%) and generally in the geostrophic balance.

The sub-halocline, quasi-steady northward (towards Fårö sill) gravity current with a width of 10–30 km was detected by the simulation. The finding was supported by the Argo float displacement data. This important deeper limb of the Baltic Sea haline conveyor belt was stronger in the case of northerly winds and weaker during south-westerlies. More detailed studies of the dynamics and water properties of this current are essential to understand the renewal process of deep layer waters in the Northern Baltic Proper and in the Gulf of Finland.

Generally, the structure of boundary current was well reproduced by the GETM. However, the meridional component of the simulated current was biased southward. Further *in-situ* measurements and simulations of the current regimes in various locations during the periods of quasi-steady forcing could help to reveal the causes of the discrepancy.

Code availability. Scripts to analyze the results are available upon request. Please contact Taavi Liblik.

Autor contributions. TL led the analyses of the data and writing of the paper with contributions from GV, JL, UL, KS and MJL. TL was responsible for the measurements and data processing, and GV for the modeling activities. KS processed the glider data.

Competing interests. The authors declare that they have no conflict of interests.

Acknowledgements. We would like to thank our colleagues and research vessels Salme crew for all the support in measurements and operations at sea. The computing time from high-performance computing center at Tallinn University of Technology and University of Tartu are gratefully acknowledged. GETM community at Leibniz Institute of Baltic Sea Reasearch are gratefully acknowledged for maintaining and developing the code.

Financial support. This work was supported by the Estonian Research Council grant PRG602. Collection of the data was financially supported by the European Regional Development Fund within National Programme for Addressing Socio-Economic Challenges through R&D (RITA). Infrastructure assets used in the current study are part of the JERICO infrastructure and supported by the JERICO-S3 project under the European Union's Horizon 2020 research and innovation programme with grant number 871153.

766

767

References

769 Berden, G., Charo, M., Möller, O. O., & Piola, A. R. (2020). Circulation and Hydrography in the
770   Western South Atlantic Shelf and Export to the Deep Adjacent Ocean: 30°S to 40°S. *Journal of*
771   *Geophysical Research: Oceans*, *125*(10), e2020JC016500.
772   https://doi.org/10.1029/2020JC016500

773 Book, J., Perkins, H., Signell, R., & Wimbush, M. (2007). The Adriatic Circulation Experiment
774   winter 2002/2003 mooring data report: a case study in ADCP data processing. In *U.S. Naval*
775   *Res. Lab. Stennis Space Center*.

776 Burchard, H., & Bolding, K. (2002). *GETM – a general estuarine transport model. Scientific*
777   *Documentation. Technical report EUR 20253 en. In: Tech. Rep. European Commission*.

778 Carstensen, J., Andersen, J. H., Gustafsson, B. G., & Conley, D. J. (2014). Deoxygenation of the
779   baltic sea during the last century. *Proceedings of the National Academy of Sciences of the*
780   *United States of America*, *111*(15), 5628–5633. https://doi.org/10.1073/pnas.1323156111

781 Csanady, G. T. (1981). Circulation in the Coastal Ocean. *Advances in Geophysics*, *23*(C), 101–183.
782   https://doi.org/10.1016/S0065-2687(08)60331-3

783 Dargahi, B. (2019). Dynamics of vortical structures in the Baltic Sea. *Dynamics of Atmospheres and*
784   *Oceans*, *88*, 101117. https://doi.org/10.1016/j.dynatmoce.2019.101117

785 Davis, R. E. (2010). On the coastal-upwelling overturning cell. *Journal of Marine Research*, *68*(3–4),
786   369–385. https://doi.org/10.1357/002224010794657173

787 Döös, K., Meier, H. E. M., & Döscher, R. (2004). The Baltic Haline Conveyor Belt or The
788   Overturning Circulation and Mixing in the Baltic. *AMBIO: A Journal of the Human*
789   *Environment*, *33*(4), 261–266. https://doi.org/10.1579/0044-7447-33.4.261

790 Ekman, V. W. (1905). On the influence of the earth's rotation on ocean currents. *Arkiv. Mat., Astron.*
791   *Fys.*, *11*, 1–52.

792 Elken, J., Raudsepp, U., & Lips, U. (2003). On the estuarine transport reversal in deep layers of the
793   Gulf of Finland. *Journal of Sea Research*, *49*(4), 267–274. https://doi.org/10.1016/S1385-
794   1101(03)00018-2

795 Geyer, W. R., & MacCready, P. (2014). The Estuarine Circulation. *Annual Review of Fluid*
796   *Mechanics*, *46*(1), 175–197. https://doi.org/10.1146/annurev-fluid-010313-141302

797 Giddings, S. N., & MacCready, P. (2017). Reverse Estuarine Circulation Due to Local and Remote
798   Wind Forcing, Enhanced by the Presence of Along-Coast Estuaries. *Journal of Geophysical*
799   *Research: Oceans*, *122*(12), 10184–10205. https://doi.org/10.1002/2016JC012479

800 Gilcoto, M., Largier, J. L., Barton, E. D., Piedracoba, S., Torres, R., Graña, R., Alonso-Pérez, F.,
801   Villacieros-Robineau, N., & de la Granda, F. (2017). Rapid response to coastal upwelling in a

semienclosed bay. *Geophysical Research Letters*, *44*(5), 2388–2397. https://doi.org/10.1002/2016GL072416

Golenko, M., Krayushkin, E., & Lavrova, O. (2017). Современные проблемы дистанционного зондирования Земли из космоса. *Current Problems in Remote Sensing of the Earth from Space.*, 280–296. https://doi.org/10.21046/2070-7401-2017-14-7-280-296

Hagen, E., & Feistel, R. (2004). Observations of low-frequency current fluctuations in deep water of the Eastern Gotland Basin/Baltic Sea. *Journal of Geophysical Research: Oceans*, *109*(C3). https://doi.org/10.1029/2003JC002017

Hagen, Eberhard, & Feistel, R. (2007). Synoptic changes in the deep rim current during stagnant hydrographic conditions in the Eastern Gotland Basin, Baltic Sea. *Oceanologia*, *49*(2), 185–208.

Hersbach, H., Bell, B., Berrisford, P., Hirahara, S., Horányi, A., Muñoz-Sabater, J., Nicolas, J., Peubey, C., Radu, R., Schepers, D., Simmons, A., Soci, C., Abdalla, S., Abellan, X., Balsamo, G., Bechtold, P., Biavati, G., Bidlot, J., Bonavita, M., … Thépaut, J.-N. (2020). The ERA5 global reanalysis. *Quarterly Journal of the Royal Meteorological Society*, *146*(730), 1999–2049. https://doi.org/10.1002/QJ.3803

Hinrichsen, H. H., von Dewitz, B., & Dierking, J. (2018). Variability of advective connectivity in the Baltic Sea. *Journal of Marine Systems*, *186*, 115–122. https://doi.org/10.1016/j.jmarsys.2018.06.010

Holtermann, P. L., Prien, R., Naumann, M., Mohrholz, V., & Umlauf, L. (2017). Deepwater dynamics and mixing processes during a major inflow event in the central Baltic Sea. *Journal of Geophysical Research: Oceans*, *122*(8), 6648–6667. https://doi.org/10.1002/2017JC013050

Jakobsen, F., Hansen, I. S., Ottesen Hansen, N. E., & Østrup-Rasmussen, F. (2010). Flow resistance in the Great Belt, the biggest strait between the North Sea and the Baltic Sea. *Estuarine, Coastal and Shelf Science*, *87*(2), 325–332. https://doi.org/10.1016/j.ecss.2010.01.014

Janssen, F., Schrum, C., & Backhaus, J. O. (1999). A climatological data set of temperature and salinity for the Baltic Sea and the North Sea. *Deutsche Hydrographische Zeitschrift*, *51*(S9), 5–245. https://doi.org/10.1007/BF02933676

Jedrasik, J., Cieślikiewicz, W., Kowalewski, M., Bradtke, K., & Jankowski, A. (2008). 44 Years Hindcast of the sea level and circulation in the Baltic Sea. *Coastal Engineering*, *55*(11), 849–860. https://doi.org/10.1016/j.coastaleng.2008.02.026

Jędrasik, J., & Kowalewski, M. (2019). Mean annual and seasonal circulation patterns and long-term variability of currents in the Baltic Sea. *Journal of Marine Systems*, *193*, 1–26. https://doi.org/10.1016/j.jmarsys.2018.12.011

Jönsson, B., Döös, K., Nycander, J., & Lundberg, P. (2008). Standing waves in the Gulf of Finland and their relationship to the basin-wide Baltic seiches. *Journal of Geophysical Research*, *113*(C3), C03004. https://doi.org/10.1029/2006JC003862

Krayushkin, E., Lavrova, O., & Strochkov, A. (2019). Application of GPS/GSM Lagrangian mini-drifters for coastal ocean dynamics analysis. *Russian Journal of Earth Sciences*, *19*(1).

840   https://doi.org/10.2205/2018ES000642

841   Leppäranta, M., & Myrberg, K. (2009). Circulation. In *Physical Oceanography of the Baltic Sea* (pp.
842   131–187). Springer Berlin Heidelberg. https://doi.org/10.1007/978-3-540-79703-6_5

843   Liblik, T., Laanemets, J., Raudsepp, U., Elken, J., & Suhhova, I. (2013). Estuarine circulation
844   reversals and related rapid changes in winter near-bottom oxygen conditions in the Gulf of
845   Finland, Baltic Sea. *Ocean Science*, *9*, 917–930.

846   Liblik, T., Naumann, M., Alenius, P., Hansson, M., Lips, U., Nausch, G., Tuomi, L., Wesslander, K.,
847   Laanemets, J., & Viktorsson, L. (2018). Propagation of Impact of the Recent Major Baltic
848   Inflows From the Eastern Gotland Basin to the Gulf of Finland. *Frontiers in Marine Science*, *5*,
849   222. https://doi.org/10.3389/fmars.2018.00222

850   Liblik, T., Väli, G., Lips, I., Lilover, M.-J., Kikas, V., & Laanemets, J. (2020). The winter
851   stratification phenomenon and its consequences in the Gulf of Finland, Baltic Sea. *Ocean
852   Science*, *16*, 1475–1490.

853   Lilover, M.-J., Elken, J., Suhhova, I., & Liblik, T. (2017). Observed flow variability along the
854   thalweg, and on the coastal slopesof the Gulf of Finland, Baltic Sea. *Estuarine, Coastal and
855   Shelf Science*, *195*, 23–33.

856   Lilover, M.-J., Pavelson, J., & Kõuts, T. (2011). Wind forced currents over the shallow naissaar Bank
857   in the Gulf of Finland. In *Boreal environment research* (Vol. 16).

858   Longdill, P. C., Healy, T. R., & Black, K. P. (2008). Transient wind-driven coastal upwelling on a
859   shelf with varying width and orientation. *New Zealand Journal of Marine and Freshwater
860   Research*, *42*(2), 181–196. https://doi.org/10.1080/00288330809509947

861   Macdonald, A. M. (1998). The global ocean circulation: a hydrographic estimate and regional
862   analysis. *Progress in Oceanography*, *41*(3), 281–382. https://doi.org/10.1016/S0079-
863   6611(98)00020-2

864   Matthäus, W., & Franck, H. (1992). Characteristics of major Baltic inflows—a statistical analysis.
865   *Continental Shelf Research*, *12*(12), 1375–1400. https://doi.org/doi:10.1016/0278-
866   4343(92)90060-W

867   McDougall, T. J., & Barker, P. M. (2011). Getting started with TEOS-10 and the Gibbs Seawater
868   (GSW) Oceanographic Toolbox. *SCOR/IAPSO WG127*, 28pp. https://doi.org/ISBN 978-0-646-
869   55621-5

870   Meier, H. E. . (2007). Modeling the pathways and ages of inflowing salt- and freshwater in the Baltic
871   Sea. *Estuarine, Coastal and Shelf Science*, *74*(4), 610–627.
872   https://doi.org/10.1016/J.ECSS.2007.05.019

873   Mohrholz, V. (2018). Major Baltic Inflow Statistics – Revised. *Frontiers in Marine Science*, *5*, 384.
874   https://doi.org/10.3389/fmars.2018.00384

875   Ollitrault, M., & Rannou, J.-P. (2013). *ANDRO: An Argo-based deep displacement dataset*.
876   https://doi.org/http://doi.org/10.17882/47077

877 Placke, M., Meier, H. E. M., Gräwe, U., Neumann, T., Frauen, C., & Liu, Y. (2018). Long-Term
878   Mean Circulation of the Baltic Sea as Represented by Various Ocean Circulation Models.
879   *Frontiers in Marine Science*, *5*(SEP), 287. https://doi.org/10.3389/fmars.2018.00287

880 Rasmus, K., Kiirikki, M., & Lindfors, A. (2015). Long-term field measurements of turbidity and
881   current speed in the Gulf of Finland leading to an estimate of natural resuspension of bottom
882   sediment. *Boreal Environment Research* , *20*, 735–747.
883   http://www.borenv.net/BER/pdfs/ber20/ber20-735.pdf

884 Reissmann, J. H., Burchard, H., Feistel, R., Hagen, E., Lass, H. U., Mohrholz, V., Nausch, G.,
885   Umlauf, L., & Wieczorek, G. (2009). Vertical mixing in the Baltic Sea and consequences for
886   eutrophication - A review. In *Progress in Oceanography* (Vol. 82, Issue 1, pp. 47–80).
887   https://doi.org/10.1016/j.pocean.2007.10.004

888 Rubio, A., Gomis, D., Jordà, G., Espino, M., Rubio, A., Gomis, D., Jordà, G., & Espino, M. (2009).
889   Estimating geostrophic and total velocities from CTD and ADCP data: Intercomparison of
890   different methods. *JMS*, *77*(1), 61–76. https://doi.org/10.1016/J.JMARSYS.2008.11.009

891 Scully, M. E. (2016). Mixing of dissolved oxygen in Chesapeake Bay driven by the interaction
892   between wind-driven circulation and estuarine bathymetry. *Journal of Geophysical Research:*
893   *Oceans*, *121*(8), 5639–5654. https://doi.org/10.1002/2016JC011924

894 Siiriä, S., Roiha, P., Tuomi, L., Purokoski, T., Haavisto, N., & Alenius, P. (2019). Applying area-
895   locked, shallow water Argo floats in Baltic Sea monitoring. *Journal of Operational*
896   *Oceanography*, *12*(1), 58–72. https://doi.org/10.1080/1755876X.2018.1544783

897 Sokolov, A., & Chubarenko, B. (2012). Wind Influence on the Formation of Nearshore Currents in
898   the Southern Baltic: Numerical Modelling Results. *Archives of Hydroengineering and*
899   *Environmental Mechanics*, *59*(1–2), 37–48. https://doi.org/10.2478/v10203-012-0003-3

900 Soomere, T., & Keevallik, S. (2001). Anisotropy of moderate and strong winds in the Baltic Proper.
901   In *Proc. Estonian Acad. Sci. Eng* (Vol. 7, Issue 1). http://kirj.ee/public/va_te/t50-1-3.pdf

902 Suhhova, I., Liblik, T., Lilover, M.-J., & Lips, U. (2018). A descriptive analysis of the linkage
903   between the vertical stratification and current oscillations in the Gulf of Finland. *Boreal*
904   *Environment Researchesearch*, *23*, 83–103.

905 Suhhova, I., Pavelson, J., & Lagemaa, P. (2015). Variability of currents over the southern slope of
906   the Gulf of Finland. *Oceanologia*, *57*(2), 132–143. https://doi.org/10.1016/j.oceano.2015.01.001

907 Umlauf, L., Arneborg, L., Umlauf, L., & Arneborg, L. (2009). Dynamics of Rotating Shallow
908   Gravity Currents Passing through a Channel. Part I: Observation of Transverse Structure.
909   *Journal of Physical Oceanography*, *39*(10), 2385–2401. https://doi.org/10.1175/2009JPO4159.1

910 Umlauf, L., & Burchard, H. (2005). Second-order turbulence closure models for geophysical
911   boundary layers. A review of recent work. *Continental Shelf Research*, *25*, 795–827.
912   https://doi.org/10.1016/j.csr.2004.08.004

913 Väli, G., Meier, H. E. M., & Elken, J. (2013). Simulated halocline variability in the Baltic Sea and its
914   impact on hypoxia during 1961-2007. *Journal of Geophysical Research: Oceans*, *118*(12),

915   6982–7000. https://doi.org/10.1002/2013JC009192

916   Villacieros-Robineau, N., Herrera, J. L., Castro, C. G., Piedracoba, S., & Roson, G. (2013).
917   Hydrodynamic characterization of the bottom boundary layer in a coastal upwelling system (Ría
918   de Vigo, NW Spain). *Continental Shelf Research*, *68*, 67–79.
919   https://doi.org/10.1016/j.csr.2013.08.017

920   Wu, H., Deng, B., Yuan, R., Hu, J., Gu, J., Shen, F., Zhu, J., Zhang, J., Wu, H., Deng, B., Yuan, R.,
921   Hu, J., Gu, J., Shen, F., Zhu, J., & Zhang, J. (2013). Detiding Measurement on Transport of the
922   Changjiang-Derived Buoyant Coastal Current. *Journal of Physical Oceanography*, *43*(11),
923   2388–2399. https://doi.org/10.1175/JPO-D-12-0158.1

924   Wu, J. (1980). Wind-Stress coefficients over Sea surface near Neutral Conditions—A Revisit.
925   *Journal of Physical Oceanography*, *10*(5), 727–740. https://doi.org/10.1175/1520-
926   0485(1980)0102.0.co;2

927   Zhurbas, V., Elken, J., Paka, V., Piechura, J., Väli, G., Chubarenko, I., Golenko, N., & Shchuka, S.
928   (2012). Structure of unsteady overflow in the supsk furrow of the baltic sea. *Journal of
929   Geophysical Research: Oceans*, *117*(4), 4027. https://doi.org/10.1029/2011JC007284

930   Zhurbas, V., Väli, G., Golenko, M., & Paka, V. (2018). Variability of bottom friction velocity along
931   the inflow water pathway in the Baltic Sea. *Journal of Marine Systems*, *184*, 50–58.
932   https://doi.org/10.1016/J.JMARSYS.2018.04.008

933   Zhurbas, V., Väli, G., & Kuzmina, N. (2021). Striped texture of submesoscale fields in the
934   northeastern Baltic Proper: Results of very high-resolution modelling for summer season.
935   *Oceanologia*. https://doi.org/10.1016/J.OCEANO.2021.08.003

936